A three-dimensional phenomenological model describing cyclic behavior of shape memory alloys

L. Petrini[a,*], A. Bertini[a]

[a] *Department of Civil and Environmental Engineering, Politecnico di Milano*

Abstract

Nowadays, shape memory alloys, in particular Nickel-Titanium alloys (NiTi), are widely adopted in many fields (biomedical, aerospace, automotive, civil ...) for producing devices exploiting pseudo-elasticity or shape memory effect. These devices are often subjected to cyclic loadings and sometimes to large deformations that modify the material response inducing functional fatigue and/or plastic strains. Accordingly, the device effectiveness is limited or even completely compromised. In this paper, a model able to take into account both the phenomena is presented. Aiming to propose this model for the design and assessment of cyclically loaded devices by finite element simulations, a phenomenological approach was used, introducing internal variables able to describe the accumulation of inelastic strains due to fatigue and plasticity and assuming that their evolution law affects also the phase transformation domain amplitude. Two limit functions was introduced for defining the phase transformation domain and plastic region. The discrete formulation of the model is also presented. Peculiar attention is posed on the material model parameteres and the procedure to calibrate them. Initially, a *driver* code was written in MATLAB for verifying the algorithm correctness and effectiveness; successively, the model was implemented by a user subroutine in a commercial finite element code. The results of several numerical tests are reported in order to show the model functionality

*Corresponding author. Address: Department of Civil and Environmental Engineering, Politecnico di Milano, Piazza Leonardo da Vinci 32, Milan, Italy. Tel. +39-02-23994307.

Email address: lorenza.petrini@polimi.it (L. Petrini)

and stability under different loading conditions. Finally, the model capability of reproducing 1D and 3D experimental tests is shown by comparison of numerical results with experimental tests published in the literature.

Keywords: Ni-Ti alloy, Nitinol, fatigue, plasticity, permanent inelasticity

1. Introduction

During last decades shape memory alloys (SMA) revealed themselves as a very promising set of materials (Srinivasan and McFarland, 2001) with a great technological potential which motivates their usage in several fields of applications. A non-exhaustive list of typical industrial fields is biomedical, aerospace, automotive, structural and robotics (Mohd Jani et al., 2014; Lecce and Concolio, 2014).

The SMA attractiveness is based upon their peculiar behavior, which shows a stress-induced, diffusionless, thermoelastic martensitic transformation between two solid phases: the austenite (A), with a high symmetric crystallographic configuration, stable at higher temperatures ($T > A_f$ = austenitic phase transformation finish temperature), and the martensite (M), with a less symmetric configuration typical of lower temperatures ($T < M_f$ = martensitic phase transformation finish temperature). Commonly, martensite shows a multiple variant configuration (M_{MV}); however stress may induces the alignment of variants giving a single-variant configuration (M_{SV}). A consequence of the existence of these two phases at the microscopic level is that SMA exhibit two macroscopic behaviors: i) the pseudo-elasticity (Otsuka and Wayman, 1998), i.e. the recovery of large deformations in loading-unloading cycles occurring at temperature higher than A_f and ii) the shape-memory effect (Duerig et al., 1990), i.e. the capability to bear large mechanically induced strains at temperature lower than M_f and to recover the original undeformed macroscopic shape with a thermal cycle (increasing the temperature up to A_f and decreasing again to M_f). Pseudo-elasticity (PE) is due to forward transformation from A to M_{SV} dur-

ing loading and inverse transformation ($M_{SV} \rightarrow A$) during unloading. Shape memory effect (SME) is due to forward transformation from M_{MV} to M_{SV} during loading and thermo-induced inverse transformation ($M_{SV} \rightarrow A$) after unloading. The stresses at which phase transformations start are different and they remain almost constant during the process: thus, stress-strain curves show hysteresis cycles.

Referring to biomedical applications, SMA and in particular Nickel-Titanium alloys (NiTi) are commonly adopted for producing minimally invasive devices exploiting pseudo-elasticity, like in the case of self-expandable stents, aortic valves, stent-grafts, endodontic rotating drills, and shape memory effect like in the case of microactuators in robotic tools, micro-pumps and surgical instrumentation (Yoneyama and Miyazaki, 2009; Petrini and Migliavacca, 2011)

The use of NiTi in these applications, instead of other standard materials (as stainless steel and cobalt-chromium), has improved their efficacy. However, all the cited devices are subjected to cyclic loadings (due to blood pulsatility or leg or vessel movements or repeating procedures) and sometimes to very large deformations (due to the crimping procedure or physiological tortuous path or overloads). In both cases inelastic strains are developed into the material. In particular, during repeated loading-unloading thermo-mechanical cycles, SMA are subjected to functional fatigue, also called transformation induced plasticity (TRIP), i.e. a decrease in the functional properties due to the accumulation of dislocations, grain boundary mismatches, and other defects produced in transformations (Eggeler et al., 2004; Lagoudas and Entchev, 2004). Moreover, large deformations and hence high stresses may induce material yielding, i.e. macroscopic plasticity associated with slip (Yan et al., 2003; Rebelo et al., 2011). Accordingly, the design procedure may be strongly improved by the knowledge of these phenomena trough experimental studies and by the use of computational models able to describe them.

From the experimental point of view the effects of thermo-mechanical cycling on the functional properties of NiTi were studied in the pioneering works of Melton and Mercier (1979), Miyazaki et al. (1986), Stachowiak and McCormick (1988).

However, it is in the last twenty years, with the production growth of devices exploiting PE and SME, that most of the experimental investigations were carried out, considering single crystalline (Gall et al., 2001; Sehitoglu et al., 2001; Gall and Maier, 2002) and polycristalline samples (Miller and Lagoudas, 2000; Morgan and Friend, 2001; Brinson et al., 2004; Nemat-Nasser and Guo, 2006; Li et al., 2009; Kang et al., 2009; Delville et al., 2011; Kang et al., 2012; Mammano and Dragoni, 2014; Kan et al., 2016) under uniaxial as well as multi-axial loading conditions (Song et al., 2014; Wang et al., 2010), potentially inducing plastic deformation associated with slip (Wang et al., 2008; Darren J. Hartl, 2008), and also using ad hoc techniques, as synchrotron X–ray diffraction, for investigating micromechanics response (Sedmak et al., 2015). The macroscopic effects of functional fatigue due to pseudoelastic cycling are: i) accumulation of residual strain, ii) decrease of the transformation stress plateau levels and change of the shape of the stress-strain curve from "plateau type" to "hardening type", iii) reduction of the stress hysteresis due to a smaller decrease of the unloadig plateau with respect to the loading one (Delville et al., 2011). Also in the case of shape memory effect, cycles induce accumulation of irrecoverable strain and increase of the plateau slope (Miller and Lagoudas, 2000).

From the NiTi constitutive modeling point of view there is a vast literature (Khandelwal and Buravalla, 2009), starting from '80s (Müller and Wilmanski, 1980; Falk, 1983; Tanaka et al., 1986) and continuously growing also during the last years. Some interesting reviews are available in the literature, that allow to have a clear figure of the evolution process in SMA modelling. Accordingly, we recall the less recent works of Patoor et al. (2006), about single crystal SMA models, Lagoudas et al. (2006), about micromechanics-based and phenomenological constitutive models of polycristalline SMA and Reese and Christ (2008), about fully 3D SMA models, as well as the up-to-date reviews of Cisse et al. (2016a,b), where an overview of the key models nowadays available, categorized in terms of the used approach in describing SMA behavior and a more specific discussion of the models able to catch complex phenomena (included TRIP and yielding) are reported, respectively.

In this paper the attention is focused on the phenomenological constitutive models describing the macroscopic thermomechanical response of polycrystalline SMA, because more suitable to be implemented in finite element codes and used for predicting the performance of cyclically loaded biomedical devices. Among the others, we recall the models of Tanaka et al. (1995), Lagoudas and Entchev (2004), Zaki and Moumni (2007), Saint-Sulpice et al. (2009), Kan and Kang (2010), Morin et al. (2011a), Morin et al. (2011b), Yu et al. (2014), Yu et al. (2015) and Yu et al. (2017), able to efficacely describe the SMA functional fatigue, the models of Yan et al. (2003), Paiva et al. (2005), Hartl and Lagoudas (2009), Zaki et al. (2010) and Zhou (2012), able to take into account material yielding and the models of Hartl et al. (2010) and Chemisky et al. (2014) focused on viscoplasticity. Complex thermo-mechanical loadings are described by Saleeb et al. (2011), Lagoudas et al. (2012), Zaki (2012), Sedlák et al. (2012), Chatziathanasiou et al. (2016) and Malagisi et al. (2017).

Having in mind to include in one model TRIP and material yielding, we decided to refer in particular to the works of Auricchio et al. (2007) and Barrera et al. (2014): starting from the phenomenological model initially proposed by Souza et al. (1998) and then improved and numerically implemented by Auricchio and Petrini (2004), Auricchio et al. (2007) and Barrera et al. (2014) have suggested some modifications to include functional fatigue and plasticity. Both the developed models show simplicity in the mathematical formulation, robustness in the solution algorithm and dependence on a relatively small number of parameters like for the original model, adding some improvements but without giving a completely satisfying description of the TRIP and yielding phenomena. In this work, we propose an evolution of the formulations developed by Auricchio et al. (2007) and Barrera et al. (2014). According to them, even if several interesting models have been proposed to describe SMA behaviour taking into account large strains (Auricchio and Taylor, 1997; Ziólkowski, 2007; Christ and Reese, 2009; Thamburaja, 2010; Arghavani et al., 2011; Zaki, 2012; Stupkiewicz and Petryk, 2013; Teeriaho, 2013), in the presented model a small strain approach was preferred, considering also that in material experimental tests commonly

performed the imposed strains not overcoms $10-12\%$. However, when devices are studied, large changes in configuration cannot be disregarded (Christ and Reese, 2008; Sakhaei and Thamburaja, 2017): for these cases we refer to Hartl and Lagoudas (2009) that showed the implementation of a finite strain model can be avoided coupling the small strain model with the capability of finite element codes to follow distortions rotating all the internal tensorial variables at each time step.

The paper is organized in the following way. In Section 2 the models used as starting point for the new formulation are presented. In Sections 3 and 4 the continuous and discrete formulations of the proposed model are described, respectively, referring both to PE and SME. However, in the remainder of the paper attention is mainly focused on pseudo-elastic effect, being the most commonly exploited in biomedical devices. Accordingly, in Section 5 the procedure to calibrate material model parameters for PE is presented, while in Section 6 an accurate sensitivity analysis of these parameters is performed. A *driver* code was written in MATLAB (MATLAB, 2016) and used to check the effectiveness of the considered models in solving stress/strain driven homogenized problems (Section 2) and to verify our proposal (Section 6). Finally, the model was implemented through a user subroutine in the finite element commercial code ABAQUS (Simulia, 2018) and the predictive capability of three-dimensional stress-states during cyclic tests was verified (Section 7)

2. Background

In this section the phenomenological model proposed by Souza et al. (1998) and then improved by Auricchio and Petrini (2004) (in the following named Souza-Auricchio-Petrini model or SAP model) is briefly summarized. The modifications introduced by Auricchio et al. (2007) and Barrera et al. (2014) in their models (in the following Auricchio and Barrera models), for taking into account fatigue and plasticity, are presented and the limitations discussed.

2.1. The Souza-Auricchio-Petrini model

The Souza-Auricchio-Petrini (SAP) model is developed in small strain regime and assumes the decompositions between deviatoric and volumetric parts for strain (Eq. (1)) and stress (Eq. (2)).

$$\boldsymbol{\varepsilon} = \mathbf{e} + \mathbf{1}\,\frac{\theta}{3} \tag{1}$$

$$\boldsymbol{\sigma} = \mathbf{s} + \mathbf{1}\,p \tag{2}$$

In the previous relations $\boldsymbol{\varepsilon}$ is the total small strain tensor, $\mathbf{e}$ its deviatoric part, $\mathbf{1}$ the second order identity tensor, θ the volumetric strain defined as $\theta = \boldsymbol{\varepsilon} : \mathbf{1}$, $\boldsymbol{\sigma}$ the Cauchy stress tensor, $\mathbf{s}$ its deviatoric part and p the hydrostatic pressure defined as $p = \boldsymbol{\sigma} : \mathbf{1}/3$.

The model considers as control variables (input) the absolute temperature T and total strain $\boldsymbol{\varepsilon}$, and provides as output the correspondent state of stress ($\boldsymbol{\sigma}$). Another second order tensor, $\mathbf{e}^{tr}$, is used as internal variable and represents the strain associated to phase transformation: it is a traceless tensor forced to evolve in a domain which is a sphere of constant radius ε_L in the space of traceless second order tensors,

$$0 \leq \|\mathbf{e}^{tr}\| \leq \varepsilon_L \tag{3}$$

The operator $\|\cdot\|$ indicates the Euclidean norm and ε_L can be seen as a material parameter, i.e. the maximum transformation strain reached during a uniaxial tensile test.

Following phenomenological thermodynamics (Lemaitre and Chaboche, 1990), a Helmholtz energy function is expressed for a multi-grain SMA material, depending on the defined state variables:

$$\begin{aligned}\psi\left(\theta, \mathbf{e}, T, \mathbf{e}^{tr}\right) = &\frac{1}{2}K\theta^2 + G\|\mathbf{e} - \mathbf{e}^{tr}\|^2 - 3\alpha K\theta(T - T_0) \\ &+\ \tau_M(T)\|\mathbf{e}^{tr}\| + \frac{h}{2}\|\mathbf{e}^{tr}\|^2 + \mathcal{I}_{\varepsilon_L}(\mathbf{e}^{tr})\end{aligned} \tag{4}$$

In this expression the first two terms account for the elastic energy contribution, splitted in the hydrostatic and deviatoric part, where K is the bulk modulus

and G the shear modulus; the term containing the thermal expansion coefficient, α, allows to consider deformations due to temperature variations between the actual temperature T and the reference temperature T_0. $\tau_M(T)\|\mathbf{e}^{tr}\|$ is the chemical energy: $\tau_M(T)$ is defined as $< \beta(T - \mathrm{M}_f) >$, with $< \bullet >$ the positive part of the argument, and indicates a linear relationship (with slope β) between temperature above M_f and the deviatoric stress at which the forward phase transformation starts (in the following s_F^S). The term containing parameter h corresponds to the transformation strain energy due to the transformation-induced hardening and regulates the slope of the deviatoric stress–strain curve during this phenomenon. Finally $\mathcal{I}_{\varepsilon_L}(\mathbf{e}^{tr})$ is an indicator function, introduced to satisfy Equation (3) and defined as:

$$\mathcal{I}_{\varepsilon_L}(\mathbf{e}^{tr}) = \begin{cases} 0 & \text{if } \|\mathbf{e}^{tr}\| \leq \varepsilon_L \\ +\infty & \text{otherwise} \end{cases} \tag{5}$$

Following standard arguments, the constitutive equations are derived from the free energy function:

$$\begin{cases} p = \dfrac{\partial \psi}{\partial \theta} &= K\left[\theta - 3\alpha(T - T_0)\right] \\ \mathbf{s} = \dfrac{\partial \psi}{\partial \mathbf{e}} &= 2G\left(\mathbf{e} - \mathbf{e}^{tr}\right) \\ \mathbf{X} = -\dfrac{\partial \psi}{\partial \mathbf{e}^{tr}} &= \mathbf{s} - \left[\tau_M + h\|\mathbf{e}^{tr}\| + \gamma\right] \dfrac{\mathbf{e}^{tr}}{\|\mathbf{e}^{tr}\|} \end{cases} \tag{6}$$

where $\mathbf{X}$ is the relative stress tensor and depends also from γ, the subdifferential of the indicator function ($\gamma = 0$ if $\|\mathbf{e}^{tr}\| < \varepsilon_L$ and $\gamma \geq 0$ if $\|\mathbf{e}^{tr}\| = \varepsilon_L$).
Disregarding the term proposed by Auricchio and Petrini (2004) to take into account the SMA asymmetric behavior, the limit function is described by the simple equation:

$$F(\mathbf{X}) = \|\mathbf{X}\| - R \tag{7}$$

with R being the radius of the elastic domain. Accordingly, when $\|\mathbf{e}^{tr}\| \to 0$, τ_M indicates the position of the center of the elastic domain. Considering the simple case of a uniaxial tensile test, where s is the uniaxial (scalar) deviatoric stress component, during loading the forward transformation starts when $s =$

$s_F^S = \tau_M + R$, during unloading the inverse transformation ends when $s = s_I^E = \tau_M - R$. Hence, the inverse transformation is complete (psedo-elastic behavior) only if $\tau_M > R$; when $\tau_M = 0$ (i.e. $T < \mathrm{M}_f$) no inverse transformation takes place (shape memory effect). The model is completed by an associative evolution law for $\mathbf{e}^{tr}$ and Kuhn-Tucker conditions:

$$\dot{\mathbf{e}}^{tr} = \dot{\zeta}\frac{\partial F(\mathbf{X})}{\partial \mathbf{X}} \tag{8}$$

$$\dot{\zeta} \geq 0 \qquad F \leq 0 \qquad \dot{\zeta}F = 0$$

2.2. The Auricchio et al. model

Starting from the equations presented above, Auricchio et al. (2007) proposed some modifications for taking into account inelastic effects due to functional fatigue induced by cyclic loads. An additional internal variable, the functional fatigue tensor $\mathbf{q}$, was introduced to model the inelastic permanent strain representing the part of $\mathbf{e}^{tr}$ which cannot be recovered during unloading. Accordingly, the thermodynamic potential was modified as follows:

$$\begin{aligned}\psi\left(\theta, \mathbf{e}, T, \mathbf{e}^{tr}, \mathbf{q}\right) = \frac{1}{2}K\theta^2 + G\|\mathbf{e} - \mathbf{e}^{tr}\|^2 \\ + \ \tau_M(T)\|\mathbf{e}^{tr} - \mathbf{q}\| + \frac{h}{2}\|\mathbf{e}^{tr}\|^2 + \frac{H}{2}\|\mathbf{q}\|^2 - A\mathbf{e}^{tr} : \mathbf{q} + \mathcal{I}_{\varepsilon_L}(\mathbf{e}^{tr})\end{aligned} \tag{9}$$

In Equation (9) H is a saturation term aimed to block the evolution of functional fatigue after some cycles are performed, A models the degradation effect, that is the progressive shifting down of the tranformation loops due to the increase of inelastic strain for functional fatigue. The thermodynamic stress-like quantity $\mathbf{Q}$ associated to $\mathbf{q}$ is hence introduced.

$$\mathbf{Q} = -\frac{\partial \psi}{\partial \mathbf{q}} = \tau_M \frac{\mathbf{e}^{tr} - \mathbf{q}}{\|\mathbf{e}^{tr} - \mathbf{q}\|} - H\mathbf{q} + A\mathbf{e}^{tr} \tag{10}$$

Limit function and associative flow rules are chosen as follows:

$$F(\mathbf{X}, \mathbf{Q}) = \|\mathbf{X}\| + k\|\mathbf{Q}\| - R \tag{11}$$

$$\begin{aligned} \dot{\boldsymbol{e}}^{tr} &= \dot{\zeta}\frac{\partial F}{\partial \boldsymbol{X}} \\ \dot{\boldsymbol{q}} &= \dot{\zeta}\frac{\partial F}{\partial \boldsymbol{Q}} \end{aligned} \tag{12}$$

where R is the elastic domain radius and k is a scaling factor for the inelastic effects. The implementation of this model in our *driver* code allowed to highlight some limitations of Auricchio model described in the following.

As in SAP model, there is no distinction between the elastic properties of martensitic and austenitic phases. The degradation effect during cycles (Figure 1a), controlled by coefficient A, equally affects the stresses of forward and inverse phase transformations, while experimental results (Delville et al., 2011) show that the phenomenon is more evident for upper plateau. Moreover, the radius of the domain in which $\mathbf{e}^{tr}$ can move is fixed (equal to ε_L - Eq.(3)) and this assumption has an effect on the functional fatigue behavior (Figure 1b): when tensile (or compression) cycles are performed the upper and lower plateau amplitude is reduced due to inelastic strain accumulation. Once the load direction is changed, the transformation plateaus become longer than the initial ones due to the fact that material loses the memory of the accumulated inelastic strains. Finally, Auricchio model does not take into account inelastic strain due to material yielding.

2.3. The Barrera et al. model

The model proposed by Barrera et al. (2014) is an evolution of Auricchio model, with two fundamental aims:

- adding the capability to account for plasticity at high level of stress, maintaining the description of the functional fatigue accumulation;
- taking into account that, when $\mathbf{q}$ evolves, some microscopic domains, where future phase transitions are hindered, are developed inside the material. This means that functional fatigue tensor has also a role in defining the shape and size of the domain in which transformation strain $\mathbf{e}^{tr}$ moves. Modeling this aspect allows correctly catching the SMA behavior

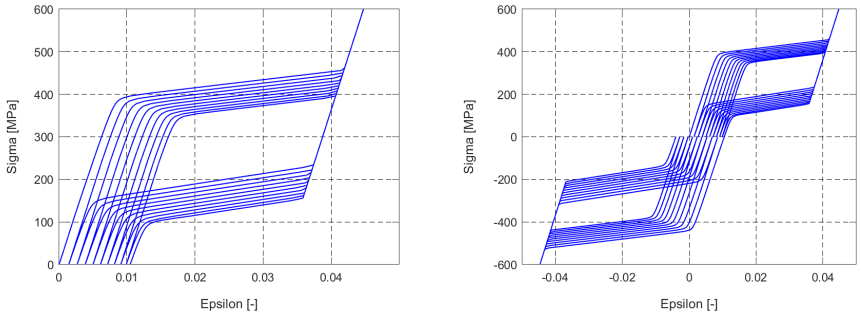

(a) (b)

Figure 1: Auricchio model. Stress-strain curves of uniaxial stress-driven loading-unloading tests: a) ten tensile cycles; b) ten tensile cycles followed by ten compression cycles. Parameters: E=50000 MPa, ν=0.35, β=3 MPa K^{-1}, T=310 K, M_f= 235 K, R=100 MPa, h=1500 MPa, ε_L= 0.04, H=25000 MPa, A=5000 MPa, k=0.02

when loading cycles in different directions (from tension to compression or viceversa) are performed.

To implement the former point, the authors introduced a new tensor, $\mathbf{e}^{pl}$, which represents the plastic strain tensor, arising at high value of applied stresses and avoiding material complete shape recovery. $\mathbf{e}^{pl}$ was assumed directly proportional to $\mathbf{q}$ ($\mathbf{e}^{pl} = a\mathbf{q}$) and hence the new definition of the elastic strain was: $\mathbf{e}^{el} = \mathbf{e} - \mathbf{e}^{tr} - a\mathbf{q}$. According to the second aim, the reduction of the transformation domain amplitude with fatigue accumulation was taken into account defining the domain as a sphere in the space of traceless symmetric tensors centered in $\mathbf{q}(t)$ having a radius varying in time, $\varepsilon_L(t_2) \leq \varepsilon_L(t_1)$, with $t_2 \geq t_1$ such that

$$\left\|\mathbf{e}^{tr}(t) - \mathbf{q}(t)\right\| \leq \varepsilon_L(t) \tag{13}$$

The added evolution law for $\varepsilon_L(t)$, given the initial value $\varepsilon_L(0) = \varepsilon_{L0}$, was:

$$\dot{\varepsilon_L}(t) = \begin{cases} -\left\|\dot{\mathbf{q}}(t)\right\| & \varepsilon_L(t) > 0 \\ 0 & \varepsilon_L(t) = 0 \end{cases} \tag{14}$$

Considering all these changes, the Helmholtz convex potential function has the following expression:

$$\psi\left(\theta, \mathbf{e}, T, \mathbf{e}^{tr}, \mathbf{q}\right) = \frac{1}{2}K\theta^2 + G\|\mathbf{e} - \mathbf{e}^{tr} - a\mathbf{q}\|^2 - 3\alpha K\theta\left(T - T_0\right) + \tau_M(T)\|\mathbf{e}^{tr} - \mathbf{q}\| + \frac{h}{2}\|\mathbf{e}^{tr} - \mathbf{q}\|^2 + \frac{H}{2}\|\mathbf{q}\|^2 + \mathcal{I}_{\varepsilon_L}(\mathbf{e}^{tr}, \mathbf{q}) \tag{15}$$

Interestingly, Barrera et al. (2014) considered three different types of norm to define the elastic domain limit surface (Eq. (11)), in terms of thermodynamic forces $\mathbf{X}$ and $\mathbf{Q}$:

- taxicab norm, $\|\mathbf{X}\| + k\|\mathbf{Q}\| - R \leq 0$. The same used in Auricchio model and characterised by a coupling of the evoution of fatigue tensor (and hence also plasticity) with the evolution of $\mathbf{e}^{tr}$.
- Euclidean norm, $\sqrt{\|\mathbf{X}\|^2 + k^2\|\mathbf{Q}\|^2} - R \leq 0$ that, respect to the previuos case, add two peculiar paths along which transformation phase and fatigue/plasticity are decoupled.
- supremum norm, $\max\{\|\mathbf{X}\|, k\|\mathbf{Q}\|\} - R \leq 0$, that allows complitely separating $\mathbf{q}$ and $\mathbf{e}^{tr}$ evolution.

The implementation of Barrera model in the *driver* showed some limitations. In case of supremum norm plasticity is corretly reproduced but not the fatigue (Fig. 2). Using taxicab norm plasticity is not reached, at least with physical values of the yielding stress, while fatigue is well described (Fig. 3): it is important to notice that the modifications applied to transformation domain $\varepsilon_L(t)$ solve limitations highlighted for Auricchio model during cyclic loading with compression/tensile stress inversion (as highlighted in Figure 3b). Euclidean norm could be the right solution, but convergence problems during simulation were found. Finally, the lack of distinction between martensite and austenite elastic modulus and a similar reduction of the upper and lower plateu levels are maintained.

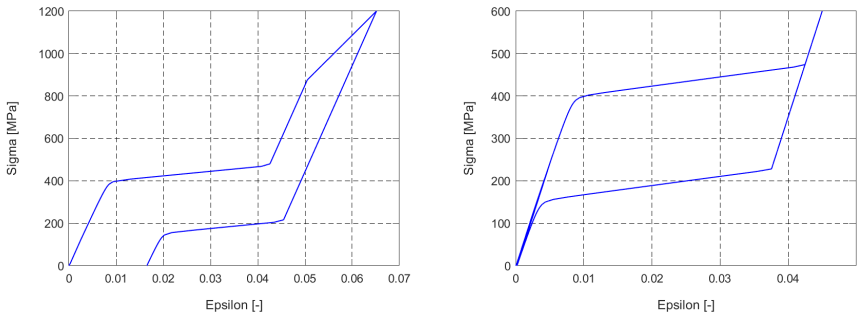

(a) (b)

Figure 2: Barrera model wth supremum norm. Stress-strain curves of uniaxial stress-driven loading-unloading tests: a) one tensile cycle above yielding stress; b) ten tensile cycles below yielding stress. Parameters: E=50000 MPa, ν=0.35, α= 10^{-6}, β=3 MPa K^{-1}, T=310 K, T_0=245 K, M_f= 235 K, R=100 MPa, h=1500 MPa, ε_L= 0.04, H=25000 MPa, a=1, k=0.1

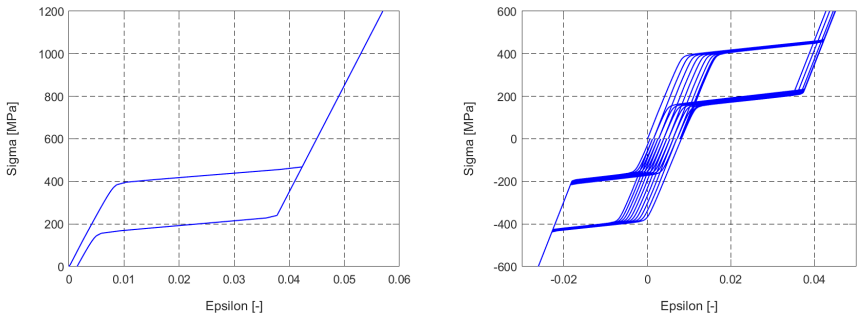

(a) (b)

Figure 3: Barrera model with taxicab norm. Stress-strain curves of uniaxial stress-driven loading-unloading tests: a) one tensile cycle above yielding stress; b) ten tensile cycles below yielding stress. Parameters: E=50000 MPa, ν=0.35, α= 10^{-6}, β=3 MPa K^{-1}, T=310 K, T_0=245 K,M_f= 235 K, R=100 MPa, h=1500 MPa, ε_L= 0.04, H=25000 MPa, a=0.5, k=0.1

3. The model formulation

Starting from modifications to SAP model proposed by Auricchio et al. (2007) and Barrera et al. (2014), a new constitutive model able to overcome their limitations has been formulated. The starting considerations are the followings:

- Auricchio model introduces a new internal variable, describing the accumulated fatigue strain, and defines a proper elastic domain such that fatigue phenomenon is caught, without influencing other aspects of the SAP model or adding further complexity to its equations.

- Barrera model considers the accumulated fatigue strain and the yielding as dependent phenomena, introducing some limitations in the model formulation.

- Experimental evidences and literature works (Wang et al., 2008; Delville et al., 2011) highlights some behaviors during tensile tests at $T > \mathrm{A}_f$ that would be useful to take into account in the model: i) at the beginning of the forward transformation ($A \rightarrow M_{SV}$) favorably oriented grains are involved and the stress-strain curve is characterized by a plateau (slope $h_1 \approx 0$), while a higher slope (h_2) characterizes the second phase of the transformation involving unfavorably oriented grains; ii) mechanical cycles may induce an increasing in the slope (h_1) of the transformation plateau; iii) after the development of plastic strain, the plateau of the inverse transformation ($M_{SV} \rightarrow A$) drops to lower stress levels.

- Experimental results show the asymmetric behaviour of SMA in tension and compression (Orgéas and Favier, 1998; Šittner et al., 2004; Thamburaja, 2005; Reedlunn et al., 2014). In the SAP model an elastic domain formulated with a Prager-Lode type limit surface was introduced. However, this approach is not sufficient to correctly catch the material response (Lim and McDowell, 1999; Bouvet et al., 2004). Moreover, the evolution of the limit domains in tension and compression during cyclic loads is even

more complex and requires an ad hoc study that is out of the scope of this work. For this reasons, as already done in Auricchio et al. (2007) and Barrera et al. (2014), in this paper the authors preferred to neglect this aspect, even if it is clearly a strong limitation of the model, considering that most of the biomedical devices are subjected to cyclic bending loads.

The proposed model uses the following control variables:

- observable: T, absolute temperature, and $\boldsymbol{\varepsilon}$, total strain.
- internal: $\mathbf{e}^{tr}$, phase transformation strain, $\mathbf{e}^{fix}$, fatigue accumulated strain representing the portion of $\mathbf{e}^{tr}$ which cannot show further phase transformations, $\mathbf{e}^{pl}$ plastic strain.

$\mathbf{e}^{fix}$ has the same function of tensor $\mathbf{q}$ in Auricchio model and, differently from Barrera model, it is assumed independent from plastic strain $\mathbf{e}^{pl}$.

To catch the experimental evidence of different slopes of the pseudo-elastic stress-strain curve during transformation from austenite to single variant martensite, it was used the proposal of Urbano and Auricchio (2015). In particular, they described the transformation-induced hardening by the slope h_1 when $\| \mathbf{e}^{tr} \| < \varepsilon_L$ (transformation plateau length) and by the slope $h_2 (\gg h_1)$ when $\| \mathbf{e}^{tr} \| \geq \varepsilon_L$, without any limitation to the norm of the transformation strain.

Two other quantities are introduced in the model to take into account the cumulative variation of fatigue and plastic strain:

$$\omega(t) = \int_0^t \left\| \dot{\boldsymbol{e}^{fix}} \right\| dt \tag{16}$$

$$\eta(t) = \int_0^t \left\| \dot{\boldsymbol{e}^{pl}} \right\| dt \tag{17}$$

For the sake of brevity, in the following we skip to report the dependency on the time t of those variables that are function of $\omega(t)$ and $\eta(t)$. Indeed, these quantities are used to take into account a linear dependency between the accumulation of inelastic strain and the slope h_1 of the transformation plateau

through the equation:

$$h_1^{'} = h_1 + h^{'}(\omega(t) + \eta(t)) \tag{18}$$

They are also used for accounting the progressive lowering of the forward and inverse transformation plateaus due to the inelastic strain accumulation. In particular, the definitions of s_F^S and s_I^E in the SAP model (Section 2.1) are modified introducing the new quantities:

$$\begin{aligned} \tau_M^{'} &= \beta\langle T - M_f\rangle - \frac{A(1+\Phi)}{2}(\omega(t) + \eta(t)) - \frac{B}{2}\eta(t) \\ R_1^{'} &= R - \frac{A(1-\Phi)}{2}(\omega(t) + \eta(t)) + \frac{B}{2}\eta(t) \end{aligned} \tag{19}$$

If only fatigue cycles are considered ($\eta(t) = 0$), it results $\tau_M^{'} + R_1^{'} = \tau_M + R - A\omega(t)$ and $\tau_M^{'} - R_1^{'} = \tau_M - R - A\Phi\omega(t)$ meaning that the upper plateau decreases of a quantity proportional to the accumulated fatigue strain and the lower one of a portion of it ($\Phi < 1$). If only plasticity is considered ($\omega(t) = 0$), it results $\tau_M^{'} + R_1^{'} = \tau_M + R - A\eta(t)$ and $\tau_M^{'} - R_1^{'} = \tau_M - R - (A\Phi + B)\eta(t)$ meaning that plasticity affects the upper plateau as fatigue but it has a stronger effect on the lowering of the unloading plateau ($B > 1$). These considerations will be used in Section 5 in order to calibrate in a simple way the material parameters. According to Barrera model, the transformation domain is considered to evolve in time. In particular, the evolution law of its radius ε_L is assumed dependent on yielding and fatigue because both phenomena concur to reduce its amplitude according to the equation:

$$\dot{\varepsilon_L}(t) = \begin{cases} -\left\|\dot{\mathbf{e}^{fix}}\right\| - b\left\|\dot{\mathbf{e}^{pl}}\right\| & \varepsilon_L(t) > 0 \\ 0 & \varepsilon_L(t) = 0 \end{cases} \tag{20}$$

with $\varepsilon_L = \varepsilon_{L0}$ at the initial time t_0. b is a scalar coefficient weighting the plastic strain effects on phase transformation domain size.

The new thermodynamic potential is given by Eq. (21), where $\boldsymbol{\xi} = \mathbf{e}^{tr} -$

$\mathbf{e}^{fix} - b\mathbf{e}^{pl}$.

$$\psi\left(\theta, \mathbf{e}, T, \mathbf{e}^{tr}, \mathbf{e}^{fix}, \mathbf{e}^{pl}\right) = \frac{1}{2}K\theta^2 + G\left\|\mathbf{e} - \mathbf{e}^{tr} - \mathbf{e}^{pl}\right\|^2 - 3\alpha K\theta\left(T - T_0\right) + \tau_M^{'}\left\|\boldsymbol{\xi}\right\| + \begin{cases} \frac{1}{2}h_1^{'}\left\|\boldsymbol{\xi}\right\|^2 - \frac{1}{2}\left(h_1^{'} + h_2\right)\left(\varepsilon_L(t) - 2\varepsilon_{L0}\right)^2 + \frac{1}{2}h_1^{'}\varepsilon_L(t)^2 & \left\|\boldsymbol{\xi}\right\| < \varepsilon_L(t) \\ \frac{1}{2}h_2\left(\left\|\boldsymbol{\xi}\right\| - \varepsilon_L(t)\right)^2 + h_1^{'}\varepsilon_L(t)\left\|\boldsymbol{\xi}\right\| - \frac{1}{2}\left(h_1^{'} + h_2\right)\left(\varepsilon_L(t) - 2\varepsilon_{L0}\right)^2 & \left\|\boldsymbol{\xi}\right\| \geq \varepsilon_L(t) \end{cases} \tag{21}$$

Deriving the potential, the obtained conjugate quantities are:

$$p = \frac{\partial\Psi}{\partial\theta} = K\left[\theta - 3\alpha\left(T - T_0\right)\right] \tag{22}$$

$$\mathbf{s} = \frac{\partial\Psi}{\partial\mathbf{e}} = 2G\left(\mathbf{e} - \mathbf{e}^{tr} - \mathbf{e}^{pl}\right) \tag{23}$$

$$\mathbf{X} = -\frac{\partial\Psi}{\partial\mathbf{e}^{tr}} = \mathbf{s} - \tau_M^{'}\frac{\boldsymbol{\xi}}{\left\|\boldsymbol{\xi}\right\|} - \begin{cases} h_1^{'}\boldsymbol{\xi} & \left\|\boldsymbol{\xi}\right\| < \varepsilon_L(t) \\ \left(h_2\boldsymbol{\xi} + \left(h_1^{'} - h_2\right)\varepsilon_L(t)\frac{\boldsymbol{\xi}}{\left\|\boldsymbol{\xi}\right\|}\right) & \left\|\boldsymbol{\xi}\right\| \geq \varepsilon_L(t) \end{cases} \tag{24}$$

$$\mathbf{Y} = -\frac{\partial\Psi}{\partial\mathbf{e}^{fix}} = \tau_M^{'}\frac{\boldsymbol{\xi}}{\left\|\boldsymbol{\xi}\right\|} + \begin{cases} h_1^{'}\boldsymbol{\xi} & \left\|\boldsymbol{\xi}\right\| < \varepsilon_L(t) \\ h_2\boldsymbol{\xi} + \left(h_1^{'} - h_2\right)\varepsilon_L(t)\frac{\boldsymbol{\xi}}{\left\|\boldsymbol{\xi}\right\|} & \left\|\boldsymbol{\xi}\right\| \geq \varepsilon_L(t) \end{cases} \tag{25}$$

$$\mathbf{Q} = -\frac{\partial\Psi}{\partial\mathbf{e}^{pl}} = \mathbf{s} + b\tau_M^{'}\frac{\boldsymbol{\xi}}{\left\|\boldsymbol{\xi}\right\|} + \begin{cases} bh_1^{'}\boldsymbol{\xi} & \left\|\boldsymbol{\xi}\right\| < \varepsilon_L(t) \\ b\left(h_2\boldsymbol{\xi} + \left(h_1^{'} - h_2\right)\varepsilon_L(t)\frac{\boldsymbol{\xi}}{\left\|\boldsymbol{\xi}\right\|}\right) & \left\|\boldsymbol{\xi}\right\| \geq \varepsilon_L(t) \end{cases} \tag{26}$$

The term $h_2\boldsymbol{\xi} + \left(h_1^{'} - h_2\right)\varepsilon_L(t)\frac{\boldsymbol{\xi}}{\left\|\boldsymbol{\xi}\right\|}$ may be rewritten as $h_2^{'}\frac{\boldsymbol{\xi}}{\left\|\boldsymbol{\xi}\right\|}$ being $h_2^{'} = h_2\left\|\boldsymbol{\xi}\right\| + \left(h_1^{'} - h_2\right)\varepsilon_L(t)$ the second slope of the transformation-induced hardening varying according to $\left\|\boldsymbol{\xi}\right\|$, $\varepsilon_L(t)$ and the cumulative variation of fatigue, $\omega(t)$, and plastic, $\eta(t)$, strains.

Assuming a two-surface model with isotropic hardening, two limit functions are introduced:

$$\begin{aligned} F_1\left(\mathbf{X}, \mathbf{Y}\right) &= \left\|\mathbf{X}\right\| + k\left\|\mathbf{Y}\right\| - R_1^{'} \leq 0 \\ F_2\left(\mathbf{Q}\right) &= \left\|\mathbf{Q}\right\| - R_2^{'} \leq 0 \end{aligned} \tag{27}$$

The former describes the transformation domain: the dimensionless parameter

k defines a scaling modulus between fatigue and transformation effects, while $R_1^{'}$ is the radius limiting the domain, previously defined. The latter describes the elastic domain (including elastic behaviour of austenite, transformation from austenite to martensite and elastic behaviour of martensite) and is limited by the radius:

$$R_2^{'} = R_2 + H_I \eta(t) + b\tau_M^{'} + \begin{cases} bh_1^{'} \left\| \boldsymbol{\xi} \right\| & \left\| \boldsymbol{\xi} \right\| < \varepsilon_L(t) \\ bh_2^{'} & \left\| \boldsymbol{\xi} \right\| \geq \varepsilon_L(t) \end{cases} \tag{28}$$

where R_2 is the material yielding limit measured during a uniaxial test up to fracture; H_I is the isotropic hardening coefficient for plastic strain. From the dissipation potential, according to an associative framework, the following flow rules for the internal variables are obtained:

$$\begin{aligned} \dot{\mathbf{e}}^{tr} &= \dot{\zeta} \frac{\mathbf{X}}{\left\| \mathbf{X} \right\|} \\ \dot{\mathbf{e}}^{fix} &= k\dot{\zeta} \frac{\mathbf{Y}}{\left\| \mathbf{Y} \right\|} \\ \dot{\mathbf{e}}^{pl} &= \dot{\mu} \frac{\mathbf{Q}}{\left\| \mathbf{Q} \right\|} \end{aligned} \tag{29}$$

with the Kuhn-Tucker conditions: $\dot{\zeta} \geq 0$, $\dot{\mu} \geq 0$, $F_1 \leq 0$, $F_2 \leq 0$, $\dot{\zeta} F_1 = 0$, $\dot{\mu} F_2 = 0$.

In the Appendix all the quantities used to define the constitutive model are listed.

We want to highlight some peculiarities of the proposed model:

- In agreement with Urbano and Auricchio (2015), two hardening parameters (h_1 and h_2) are introduced for describing the phase transformation.
- The two hardening parameters are modified in $h_1^{'}$ and $h_2^{'}$ for taking account of their linear evolution with inelastic effects, due to both plastic strain and fatigue accumulation. This aspect allows modeling the increment of the slopes during loading-unloading cycles.
- The transformation plateau amplitude ε_L decreases, based on fatigue and plastic strain accumulation.

- The deviatoric stresses of forward transformation start (s_F^S) and inverse transformation end (s_I^E) degrade proportionally to accumulated irreversible strain.

- Plastic strain evolution follows an isotropic rule.

Finally, we want to verify that the model is thermodynamically consistent. Assuming an isothermal process, we have to show that the mechanical dissipation function $\dot{\psi} - \boldsymbol{\sigma} : \dot{\boldsymbol{\varepsilon}} \leq 0$ is satisfied, at least for an evolution of the internal variables $(\boldsymbol{\varepsilon}(t), \mathbf{e}^{tr}(t), \mathbf{e}^{fix}(t), \mathbf{e}^{pl}(t), \varepsilon_L(t))$ and a thermodynamic potential $\psi(\boldsymbol{\varepsilon}(t), \mathbf{e}^{tr}(t), \mathbf{e}^{fix}(t), \mathbf{e}^{pl}(t), \varepsilon_L(t))$ sufficiently smooth. Accordingly, we need to check the inequality:

$$\begin{aligned}
&\left(\frac{\partial \psi}{\partial \boldsymbol{\varepsilon}} - \boldsymbol{\sigma}\right) : \dot{\boldsymbol{\varepsilon}} + \frac{\partial \psi}{\partial \mathbf{e}^{tr}} : \dot{\mathbf{e}^{tr}} + \frac{\partial \psi}{\partial \mathbf{e}^{fix}} : \dot{\mathbf{e}^{fix}} + \frac{\partial \psi}{\partial \mathbf{e}^{pl}} : \dot{\mathbf{e}^{pl}} + \frac{\partial \psi}{\partial \varepsilon_L} : \dot{\varepsilon_L} = \\
&- \mathbf{X} : \dot{\mathbf{e}^{tr}} - \mathbf{Y} : \dot{\mathbf{e}^{fix}} - \mathbf{Q} : \dot{\mathbf{e}^{pl}} + \frac{\partial \psi}{\partial \varepsilon_L} : \dot{\varepsilon_L} = \\
&- \dot{\zeta} \|\mathbf{X}\| - k\dot{\zeta} \|\mathbf{Y}\| - \dot{\mu} \|\mathbf{Q}\| + \frac{\partial \psi}{\partial \varepsilon_L} : \dot{\varepsilon_L} \leq 0
\end{aligned} \tag{30}$$

Considering that the first three terms of Eq. (30) are surely less than zero, we only have to show that, in the last term, $\partial\psi/\partial\varepsilon_L$ is greater than zero, since $\dot{\varepsilon_L}$ is always less than or equal to zero according to Eq. (20). It results:

$$\frac{\partial \psi}{\partial \varepsilon_L} = \begin{cases} -\left(h_1^{'} + h_2\right)(\varepsilon_L - 2\varepsilon_{L0}) + h_1^{'}\varepsilon_L & \|\boldsymbol{\xi}\| < \varepsilon_L(t) \\ -h_2\left(\|\boldsymbol{\xi}\| - \varepsilon_L\right) + h_1^{'}\|\boldsymbol{\xi}\| - \left(h_1^{'} + h_2\right)(\varepsilon_L - 2\varepsilon_{L0}) & \|\boldsymbol{\xi}\| \geq \varepsilon_L(t) \end{cases} \tag{31}$$

The condition is satisfied having numerically verified that $\|\boldsymbol{\xi}\|$ is always smaller than $2\varepsilon_{L0}$, since $\mathbf{e}^{fix}$ and $\mathbf{e}^{pl}$ start to grow up before that $\|\mathbf{e}^{tr}\|$ reaches the value $2\varepsilon_{L0}$. This was also confirmed by experimental tests.

4. The model discrete form

The developed discrete formulation of the proposed model, useful for its numerical implementation in a commercial code, is summarized in this Section. The time interval of interest $[0, T]$ is divided in substeps: in the generic interval

$[t_n, t_{n+1}]$ quantities with n subscript refer to the previous time instant while quantities with *n+1* subscript refer to actual time. At each instant of time an implicit time-discrete strain driven problem is solved. Hence, the input of the algorithm are the material parameters (see Table 4), the total strain tensor and temperature at the actual time ($\boldsymbol{\varepsilon}_{n+1}$ and T_{n+1}), the internal variables at the previous time instant ($\mathbf{e}_n^{tr}, \mathbf{e}_n^{fix}, \mathbf{e}_n^{pl}, \varepsilon_{L,n}$) and the quantities ω_n and η_n. The output at the end of the substep are the stress tensor ($\boldsymbol{\sigma}_{n+1}$) and the updated variables ($\mathbf{e}_{n+1}^{tr}, \mathbf{e}_{n+1}^{fix}, \mathbf{e}_{n+1}^{pl}, \varepsilon_{L,n+1}, \omega_{n+1}, \eta_{n+1}$). In agreement with Auricchio et al. (2007), some regularizations of $\|\boldsymbol{\xi}\|$ and $\|\mathbf{X}\|$ are introduced in the free-energy potential and limit functions using the definition:

$$\begin{aligned} \overline{\|a\|} &= \sqrt{\|a\|^2 + \delta} - \sqrt{\delta} \\ \frac{d\overline{\|a\|}}{da} &= \frac{a}{\sqrt{\|a\|^2 + \delta}} = c_1 a \end{aligned} \tag{32}$$

where δ sets the norm regularization smoothness. Equations (21) and (27) are modified as follows:

$$\begin{aligned} \psi\left(\theta, \mathbf{e}, T, \mathbf{e}^{tr}, \mathbf{e}^{fix}, \mathbf{e}^{pl}\right) &= \frac{1}{2}K\theta^2 + G\left\|\mathbf{e} - \mathbf{e}^{tr} - \mathbf{e}^{pl}\right\|^2 - 3\alpha K\theta\left(T - T_0\right) + \tau_M^{'}\overline{\|\boldsymbol{\xi}\|} \\ &+ \begin{cases} \frac{1}{2}h_1^{'}\|\boldsymbol{\xi}\|^2 - \frac{1}{2}\left(h_1^{'} + h_2\right)\left(\varepsilon_L(t) - 2\varepsilon_{L0}\right)^2 + \frac{1}{2}h_1^{'}\varepsilon_L(t)^2 & \|\boldsymbol{\xi}\| < \varepsilon_L(t) \\ \frac{1}{2}h_2\left(\|\boldsymbol{\xi}\| - \varepsilon_L(t)\right)^2 + h_1^{'}\varepsilon_L(t)\overline{\|\boldsymbol{\xi}\|} - \frac{1}{2}\left(h_1^{'} + h_2\right)\left(\varepsilon_L(t) - 2\varepsilon_{L0}\right)^2 & \|\boldsymbol{\xi}\| \geq \varepsilon_L(t) \end{cases} \end{aligned} \tag{33}$$

$$\begin{aligned} F_1\left(\mathbf{X}, \mathbf{Y}\right) &= \|\mathbf{X}\| + k\overline{\|\mathbf{Y}\|} - R_1^{'} \leq 0 \\ F_2\left(\mathbf{Q}\right) &= \|\mathbf{Q}\| - R_2^{'} \leq 0 \end{aligned} \tag{34}$$

The discretized form of the evolution laws is:

$$\begin{aligned}
\mathbf{e}^{tr}_{n+1} &= \mathbf{e}^{tr}_{n} + \Delta\zeta \frac{\mathbf{X}_{n+1}}{\|\mathbf{X}_{n+1}\|} \\
\mathbf{e}^{fix}_{n+1} &= \mathbf{e}^{fix}_{n} + k\Delta\zeta \frac{\mathbf{Y}_{n+1}}{\sqrt{\|\mathbf{Y}_{n+1}\|^2 + \delta}} \\
\mathbf{e}^{pl}_{n+1} &= \mathbf{e}^{pl}_{n} + \Delta\mu \frac{\mathbf{Q}_{n+1}}{\|\mathbf{Q}_{n+1}\|} \\
\omega_{n+1} &= \omega_n + \Delta\zeta k \\
\eta_{n+1} &= \eta_n + \Delta\mu \\
\varepsilon_{L,n+1} &= \varepsilon_{L,n} - \begin{cases} \Delta\zeta k - b\Delta\mu & \text{if} \quad \varepsilon_L > 0 \\ 0 & \text{if} \quad \varepsilon_L = 0 \end{cases}
\end{aligned} \tag{35}$$

where:

$$\begin{aligned}
\Delta\zeta &= \int_{t_n}^{t_{n+1}} \dot{\zeta} dt \\
\Delta\mu &= \int_{t_n}^{t_{n+1}} \dot{\mu} dt
\end{aligned} \tag{36}$$

To solve the equations, a typical procedure used in classic plasticity theory is employed, based on elastic predictor-inelastic corrector, according to Table 1. Two transformation phases, cases PT_1 and PT_2 have been defined corresponding to the two stress-strain curve slopes, h_1 (when $\|\boldsymbol{\xi}\| < \varepsilon_L$) and h_2 (when $\|\boldsymbol{\xi}\| \geq \varepsilon_L$), where only $\mathbf{e}^{tr}$, $\mathbf{e}^{fix}$, ω and ε_L vary. When plasticity is activated, case PL, also $\mathbf{e}^{pl}$ and η change. To improve solution convergence during inelastic step, the proposed algorithm starts from the hypothesis of no plasticity ($F_2 < 0$) and only residual equations of the variables $\mathbf{X}, \mathbf{Y}, \Delta\zeta$ are considered according to case PT_1 or PT_2 depending on $\|\boldsymbol{\xi}\|$ (see Table 2). If, at the end of this step, the yielding threshold is overcome ($F_2 > 0$), the full set of residual equations is taken into account (see Table 3).

The system of residual equations ($\mathbf{R}^X_{n+1}$, $\mathbf{R}^Y_{n+1}$ etc., see Table 2) is solved using the Newton-Rapshon algorithm, proceeding to compute new values of

Table 1: Time-discrete frame: solution algorithm.

TIME-DISCRETE MODEL FRAME

1. Compute trial state

$$\begin{cases} \mathbf{e}_{n+1}^{tr,TR} = \mathbf{e}_n^{tr} \\ \mathbf{e}_{n+1}^{fix,TR} = \mathbf{e}_n^{fix} \\ \mathbf{e}_{n+1}^{pl,TR} = \mathbf{e}_n^{pl} \\ \eta_{n+1}^{TR} = \eta_n \\ \omega_{n+1}^{TR} = \omega_n \\ \boldsymbol{\xi}_{n+1}^{TR} = \mathbf{e}_{n+1}^{tr,TR} - \mathbf{e}_{n+1}^{fix,TR} - b\mathbf{e}_{n+1}^{pl,TR} \\ \varepsilon_{L,n+1}^{TR} = \varepsilon_{L,n} \\ \mathbf{s}_{n+1}^{TR} = 2G\left(\mathbf{e}_{n+1} - \mathbf{e}_{n+1}^{tr,TR} - \mathbf{e}_{n+1}^{pl,TR}\right) \end{cases}$$

2. Check material state

if $\left\|\boldsymbol{\xi}_{n+1}^{TR}\right\| < \varepsilon_{L,n+1}^{TR}$ then

$$\text{compute:} \begin{cases} \mathbf{X}_{n+1}^{TR} = \mathbf{s}_{n+1}^{TR} - \tau_M^{'} c_1 \boldsymbol{\xi}_{n+1}^{TR} - h_1^{'} \boldsymbol{\xi}_{n+1}^{TR} \\ \mathbf{Y}_{n+1}^{TR} = \tau_M^{'} c_1 \boldsymbol{\xi}_{n+1}^{TR} + h_1^{'} \boldsymbol{\xi}_{n+1}^{TR} \\ \mathbf{Q}_{n+1}^{TR} = \mathbf{s}_{n+1}^{TR} v + b\tau_M^{'} c_1 \boldsymbol{\xi}_{n+1}^{TR} + b h_1^{'} \boldsymbol{\xi}_{n+1}^{TR} \\ F_{1,n+1}^{TR} = \left\|\mathbf{X}_{n+1}^{TR}\right\| + k\overline{\left\|\mathbf{Y}_{n+1}^{TR}\right\|} - R_{1,n+1}^{'} \\ F_{2,n+1}^{TR} = \left\|\mathbf{Q}_{n+1}^{TR}\right\| - R_{2,n+1}^{'} \end{cases}$$

elseif $\left\|\boldsymbol{\xi}_{n+1}^{TR}\right\| \geq \varepsilon_{L,n+1}^{TR}$ then

$$\text{compute:} \begin{cases} \mathbf{X}_{n+1}^{TR} = \mathbf{s}_{n+1}^{TR} - \tau_M^{'} c_1 \boldsymbol{\xi}_{n+1}^{TR} - h_2 \boldsymbol{\xi}_{n+1}^{TR} - \left(h_1^{'} - h_2\right) \varepsilon_{L,n+1}^{TR} c_1 \boldsymbol{\xi}_{n+1}^{TR} \\ \mathbf{Y}_{n+1}^{TR} = \tau_M^{'} c_1 \boldsymbol{\xi}_{n+1}^{TR} + h_2 \boldsymbol{\xi}_{n+1}^{TR} + \left(h_1^{'} - h_2\right) \varepsilon_{L,n+1}^{TR} c_1 \boldsymbol{\xi}_{n+1}^{TR} \\ \mathbf{Q}_{n+1}^{TR} = \mathbf{s}_{n+1}^{TR} + b\tau_M^{'} c_1 \boldsymbol{\xi}_{n+1}^{TR} + b\left(h_2 \boldsymbol{\xi}_{n+1}^{TR} + \left(h_1^{'} - h_2\right) \varepsilon_{L,n+1}^{TR} c_1 \boldsymbol{\xi}_{n+1}^{TR}\right) \\ F_{1,n+1}^{TR} = \left\|\mathbf{X}_{n+1}^{TR}\right\| + k\overline{\left\|\mathbf{Y}_{n+1}^{TR}\right\|} - R_{1,n+1}^{'} \\ F_{2,n+1}^{TR} = \left\|\mathbf{Q}_{n+1}^{TR}\right\| - R_{2,n+1}^{'} \end{cases}$$

endif

$$\text{check } F_{1,n+1}^{TR} \text{ and } F_{2,n+1}^{TR}: \begin{cases} \text{if } \left(F_{1,n+1}^{TR} < 0\right) \text{ and } \left(F_{2,n+1}^{TR} < 0\right) \text{ then} \\ \quad \textbf{elastic step } (EL) \\ \text{else} \\ \quad \textbf{phase transformation } (PT_1 \text{ or } PT_2) \\ \quad \textbf{or plasticity } (PL) \\ \text{end if} \end{cases}$$

3. Update material state

See Table 2

Table 2: Time-discrete frame: branch solution and state update - part 1.

BRANCH SOLUTION AND STATE UPDATE (Part 1)

if (CASE EL - Elastic step) then

$$\begin{cases} \mathbf{e}_{n+1}^{tr} = \mathbf{e}_{n+1}^{tr,TR} \\ \mathbf{e}_{n+1}^{fix} = \mathbf{e}_{n+1}^{fix,TR} \\ \mathbf{e}_{n+1}^{pl} = \mathbf{e}_{n+1}^{pl,TR} \\ \omega_{n+1} = \omega_{n+1}^{TR} \\ \eta_{n+1} = \eta_{n+1}^{TR} \\ \varepsilon_{L,n+1} = \varepsilon_{L,n+1}^{TR} \\ \boldsymbol{\xi}_{n+1} = \mathbf{e}_{n+1}^{tr} - \mathbf{e}_{n+1}^{fix} - b\mathbf{e}_{n+1}^{pl} \end{cases}$$

else if (CASE PT - Phase transformation) then

assume no active plasticity $F_{2,n+1} < 0$ ($\mathbf{e}_{n+1}^{pl} = \mathbf{e}_{n}^{pl}$ and $\eta_{n+1} = \eta_n$),

find $\mathbf{e}_{n+1}^{tr}$, $\mathbf{e}_{n+1}^{fix}$, ω_{n+1} and $\varepsilon_{L,n+1}$ solving residual equations:

if PT_1 active ($\left\|\boldsymbol{\xi}_{n+1}^{TR}\right\| < \varepsilon_{L,n+1}^{TR}$) then

$$\begin{cases} \mathbf{R}_{n+1}^{X} = \mathbf{X}_{n+1} - \mathbf{s}_{n+1}^{TR} + \tau_M^{'} c_1 \boldsymbol{\xi}_{n+1} + h_1^{'} \boldsymbol{\xi}_{n+1} = 0 \\ \mathbf{R}_{n+1}^{Y} = \mathbf{Y}_{n+1} - \tau_M^{'} c_1 \boldsymbol{\xi}_{n+1} - h_1^{'} \boldsymbol{\xi}_{n+1} = 0 \\ \mathbf{R}_{n+1}^{\Delta\zeta} = \|\mathbf{X}_{n+1}\| + k\overline{\|\mathbf{Y}_{n+1}\|} - R_{1,n+1}^{'} = 0 \end{cases}$$

check solution: $\begin{cases} \text{if } \overline{\|\boldsymbol{\xi}_{n+1}\|} < \varepsilon_{L,n+1} \text{ then} & \text{exit} \\ \text{else} & \textbf{solve CASE } PT_2 \\ \text{end if} \end{cases}$

elseif PT_2 active $\left(\left\|\boldsymbol{\xi}_{n+1}^{TR}\right\| \geq \varepsilon_{L,n+1}^{TR}\right)$ then

$$\begin{cases} \mathbf{R}_{n+1}^{X} = \mathbf{X}_{n+1} - \mathbf{s}_{n+1}^{TR} + \tau_M^{'} c_1 \boldsymbol{\xi}_{n+1} + h_2 \boldsymbol{\xi}_{n+1} + \left(h_1^{'} - h_2\right) \varepsilon_{L,n+1} c_1 \boldsymbol{\xi}_{n+1} = 0 \\ \mathbf{R}_{n+1}^{Y} = \mathbf{Y}_{n+1} - \tau_M^{'} c_1 \boldsymbol{\xi}_{n+1} - h_2 \boldsymbol{\xi}_{n+1} - \left(h_1^{'} - h_2\right) \varepsilon_{L,n+1} c_1 \boldsymbol{\xi}_{n+1} = 0 \\ \mathbf{R}_{n+1}^{\Delta\zeta} = \|\mathbf{X}_{n+1}\| + k\overline{\|\mathbf{Y}_{n+1}\|} - R_{1,n+1}^{'} = 0 \end{cases}$$

check solution: $\begin{cases} \text{if } \overline{\|\boldsymbol{\xi}_{n+1}\|} \geq \varepsilon_{L,n+1} \text{ then} & \text{exit} \\ \text{else} & \textbf{solve CASE } PT_1 \\ \text{end if} \end{cases}$

end if

check solution: $\begin{cases} \text{if } F_{2,n+1} < 0 \text{ then} & \text{exit} \\ \text{else} & \textbf{solve CASE } PL \\ \text{end if} \end{cases}$

if (CASE PL - Active plasticity) see Table 3

end if

Update $\mathbf{s}_{n+1} = 2G\left(\mathbf{e}_{n+1} - \mathbf{e}_{n+1}^{tr} - \mathbf{e}_{n+1}^{pl}\right)$

Table 3: Time-discrete frame: branch solution and state update - part 2.

BRANCH SOLUTION AND STATE UPDATE (Part 2)

if (CASE PL - Active plasticity) then

find $\mathbf{e}^{tr}_{n+1}$, $\mathbf{e}^{fix}_{n+1}$,$\mathbf{e}^{pl}_{n+1}$, ω_{n+1}, η_{n+1} and $\varepsilon_{L,n+1}$ solving residual equations:

$$\begin{cases} \mathbf{R}^{X}_{n+1} = \mathbf{X}_{n+1} - \mathbf{s}^{TR}_{n+1} + \tau^{'}_{M} c_1 \boldsymbol{\xi}_{n+1} + h_2 \boldsymbol{\xi}_{n+1} + \left(h^{'}_{1} - h_2\right) \varepsilon_{L,n+1} c_1 \boldsymbol{\xi}_{n+1} = 0 \\ \mathbf{R}^{Y}_{n+1} = \mathbf{Y}_{n+1} - \tau^{'}_{M} c_1 \boldsymbol{\xi}_{n+1} - h_2 \boldsymbol{\xi}_{n+1} - \left(h^{'}_{1} - h_2\right) \varepsilon_{L,n+1} c_1 \boldsymbol{\xi}_{n+1} = 0 \\ \mathbf{R}^{Q}_{n+1} = \mathbf{Q}_{n+1} - \mathbf{s}^{TR}_{n+1} - b\tau^{'}_{M} c_1 \boldsymbol{\xi}_{n+1} - b\left(h_2 \boldsymbol{\xi}_{n+1} + \left(h^{'}_{1} - h_2\right) \varepsilon_{L,n+1} c_1 \boldsymbol{\xi}_{n+1}\right) = 0 \\ \mathbf{R}^{\Delta\zeta}_{n+1} = \|\mathbf{X}_{n+1}\| + k\overline{\|\mathbf{Y}_{n+1}\|} - R^{'}_{1,n+1} = 0 \\ \mathbf{R}^{\Delta\mu}_{n+1} = \|\mathbf{Q}_{n+1}\| - R^{'}_{2,n+1} = 0 \end{cases}$$

variable at each iteration with the following rule:

$$\begin{bmatrix} \mathbf{X} \\ \mathbf{Y} \\ \mathbf{Q} \\ \Delta\zeta \\ \Delta\mu \end{bmatrix}_{n+1} = \begin{bmatrix} \mathbf{X} \\ \mathbf{Y} \\ \mathbf{Q} \\ \Delta\zeta \\ \Delta\mu \end{bmatrix}_{n} - R^{-1}_{n+1} \begin{bmatrix} \mathbf{R}^{X} \\ \mathbf{R}^{Y} \\ \mathbf{R}^{Q} \\ \mathbf{R}^{\Delta\zeta} \\ \mathbf{R}^{\Delta\mu} \end{bmatrix}_{n+1} \tag{37}$$

where matrix R_{n+1} contains derivatives of residual equations. Convergence is reached when residual norm satisfies the required tolerance.

Aiming to use the costitutive model as subroutine in an implicit solver of nonlinar problems, a consistent tangent fourth-order tensor $\mathbb{D}$ is also calculated:

$$\mathbb{D}_{n+1} = \frac{d\boldsymbol{\sigma}_{n+1}}{d\boldsymbol{\varepsilon}_{n+1}} = K\left(\mathbf{1}\otimes\mathbf{1}\right) + 2G\left(\mathbb{I} - \frac{d\mathbf{e}^{tr}_{n+1}}{d\mathbf{e}_{n+1}} - \frac{d\mathbf{e}^{pl}_{n+1}}{d\mathbf{e}_{n+1}}\right) = K\left(\mathbf{1}\otimes\mathbf{1}\right) + 2G\left(\mathbb{I} - \mathbb{E}_1 - \mathbb{E}_2\right)$$

where $\mathbb{I}$ is the fourth-order identity tensor. Linearizing the residual equations

of Table 3 with respect to $\mathbf{X}, \mathbf{Y}, \mathbf{Q}, \Delta\zeta, \Delta\mu$ and also $\mathbf{e}$, we obtain:

$$\begin{bmatrix} d\mathbf{X} \\ d\mathbf{Y} \\ d\mathbf{Q} \\ d\Delta\zeta \\ d\Delta\mu \end{bmatrix}_{n+1} = -R_{n+1}^{-1} \begin{bmatrix} \mathbf{R}_{,\mathbf{e}}^{X} \\ \mathbf{R}_{,\mathbf{e}}^{Y} \\ \mathbf{R}_{,\mathbf{e}}^{Q} \\ \mathbf{R}_{,\mathbf{e}}^{\Delta\zeta} \\ \mathbf{R}_{,\mathbf{e}}^{\Delta\mu} \end{bmatrix}_{n+1} : d\mathbf{e} \tag{38}$$

where $\mathbf{R}_{,\mathbf{e}}^{X}$ means the derivative of the residual equations $\mathbf{R}^{X}$ with respect to $\mathbf{e}$ and so on. Finally, linearizing $\mathbf{e}^{tr}$ and $\mathbf{e}^{pl}$ the following epressions are obtained:

$$\mathbb{E}_1 = \left[\mathbf{e}_{,X}^{tr}\, \mathbf{e}_{,Y}^{tr}\, \mathbf{e}_{,Q}^{tr}\, \mathbf{e}_{,\Delta\zeta}^{tr}\, \mathbf{e}_{,\Delta\mu}^{tr}\right]_{n+1} R_{n+1}^{-1} \begin{bmatrix} \mathbf{R}_{,\mathbf{e}}^{X} \\ \mathbf{R}_{,\mathbf{e}}^{Y} \\ \mathbf{R}_{,\mathbf{e}}^{Q} \\ \mathbf{R}_{,\mathbf{e}}^{\Delta\zeta} \\ \mathbf{R}_{,\mathbf{e}}^{\Delta\mu} \end{bmatrix}_{n+1} \tag{39}$$

$$\mathbb{E}_2 = \left[\mathbf{e}_{,X}^{pl}\, \mathbf{e}_{,Y}^{pl}\, \mathbf{e}_{,Q}^{pl}\, \mathbf{e}_{,\Delta\zeta}^{pl}\, \mathbf{e}_{,\Delta\mu}^{pl}\right]_{n+1} R_{n+1}^{-1} \begin{bmatrix} \mathbf{R}_{,\mathbf{e}}^{X} \\ \mathbf{R}_{,\mathbf{e}}^{Y} \\ \mathbf{R}_{,\mathbf{e}}^{Q} \\ \mathbf{R}_{,\mathbf{e}}^{\Delta\zeta} \\ \mathbf{R}_{,\mathbf{e}}^{\Delta\mu} \end{bmatrix}_{n+1} \tag{40}$$

5. The model parameter calibration

Model parameters can be calibrated performing a small number of experimental uniaxial tensile tests on material samples. Accordingly, in this Section, second order tensors are considered as scalar quantities and written using a not bold font. In the following the parameter calibration will be described with reference in particular to the pseudo-elastic behaviour. An experimental uniaxial tensile test up to material ultimate strength (Figure 4) allows to identify some fundamental points: stress and strain of forward transformation start (σ_F^S and ε_F^S), stress and strain of forward transformation end (σ_F^E and ε_F^E), yielding stress (σ_Y). Recalling that in the model these quantities are related to the

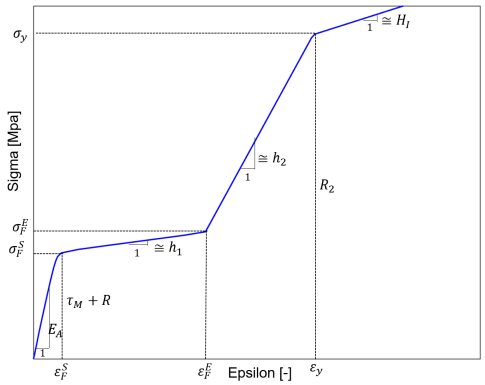

Figure 4: Stress-strain uniaxial loading curve showing the most important parameters which can be directly found.

norm of deviatoric stress and strain tensors, there is a factor of proportionality among the quantities calculated using the experimental $\sigma - \varepsilon$ curve and the input parameters of the model. In particular, the initial plateau length is given by $\varepsilon_{L0} = \sqrt{(}3/2)(\varepsilon_F^E - \varepsilon_F^S)$, the initial radius of the yield surface is $R_2 = \sqrt{(}2/3)\sigma_Y$, while the radius of the transformation domain is obtained from the relationship $\tau_M + R = \sqrt{(}2/3)\sigma_F^S$. τ_M is known once the β parameter is got from tensile tests at different temperatures calculating the slope $\frac{d\sigma}{dT}$ with $\sigma = \sigma_F^S$, and measuring the test temperature and M_f.

The initial linear tract of the experimental $\sigma - \varepsilon$ curve corresponds to austenite elastic response, so its slope represents austenite Young modulus, E_A. The other linear tracts are related to the hardening parameters through the coefficient 3/2.

Parameters regulating fatigue are calibrated performing two experimental loading-unloading tensile cycles (Figure 5) above the end of transformation plateau but below the yielding trashold ($\sigma_F^E < \sigma < \sigma_Y$). k parameter is a scaling factor between phase transformation and fatigue effects depending on the selected definition of the yield function F_1 (Eq. (27)): an estimate of its value can obtained calculating the ratio between the accumulated irreversible strain ε^{acc} (related to e_{fix}) and the global variation of the transformation strain

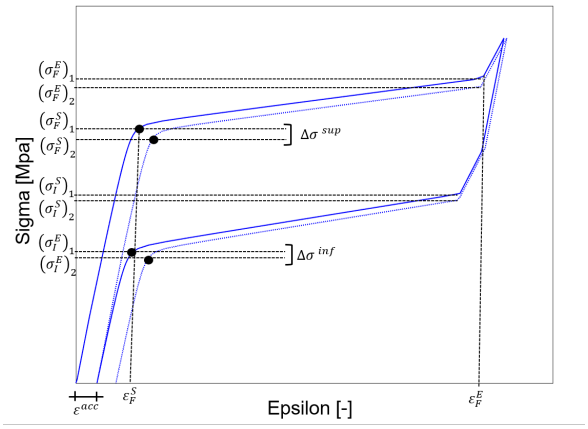

Figure 5: Two loading-unloading uniaxial cycles used for fatigue calibration. Effects of parameters A and Φ are shown.

(e_{tr}) during an experimental mechanical cycle. Considered the first cycle of the test in Figure 5, during the loading phase the transformation strain varies between 0 and $\varepsilon_F^E - \varepsilon_F^S$, during the unloading phase it varies beween $\varepsilon_F^E - \varepsilon_F^S$ and ε^{acc}. Accordingly, the scaling factor k is computed as:

$$k = \frac{\varepsilon^{acc}}{2(\varepsilon_F^E - \varepsilon_F^S) - \varepsilon^{acc}} \tag{41}$$

Degradation effect is modeled to be proportional to accumulated irreversable strain: after a loading-unloading-reloading cycle the upper plateau drop is $\Delta\sigma^{sup} = 3/2(A\varepsilon^{acc})$., while the lower plateau drop is connected to the previous one using parameter Φ, according the equation $\Delta\sigma^{inf} = \Phi\Delta\sigma^{sup}$ (Figure 5). The values of A and Φ can be simply obtained measuring from experimental curve the upper and lower plateau drops and ε^{acc}. From the same experimental test, in case the material behavior exhibits an increase in plateau slope during repeating loading-unloading cycles, we can also calibrate the parameter h', which links together slope variation during phase transformation and the entity of accumulated irreversible strain. For sake of simplicity, the slope variation is assumed linearly dependent on accumulated deformation:

$$\left(\frac{d\sigma}{d\varepsilon}\right)_{secondcycle} = \left(\frac{d\sigma}{d\varepsilon}\right)_{initial} + h'\varepsilon^{acc}\sqrt{\frac{3}{2}} \tag{42}$$

We observe that the proposed model is not able to catch not constant accumulation during loading-unloading fatigue cycles. The choice to calibrate k, A, h and Φ on the first two mechanical cycles could lead to a situation where model results and experimental evidence are similar during the first cycles, but differ in the following ones. A possible alternative is to calibrate the model on an average experimental behavior of the first 10-20 mechanical cycles. In this way the model is not able to correctly follow the initial material behavior, but its response becomes reliable in long term prevision.

The last parameters we need to calibrate the model are b and B, which are the coefficients regulating the lower plateau length reduction and drop due to plastic strain. To obtain them, a two-cycle uniaxial tensile test has to be performed reaching a stress lower than σ_F^E and a stress higher than σ_Y in the first and the second cycle, respectively (Figure 6). Parameter b represents the ratio between the accumulated inelastic strain only due to fatigue and the inelastic strain due to plasticity:

$$b = \frac{\varepsilon^{acc} - \varepsilon^{pl}}{\varepsilon^{pl}} \tag{43}$$

In this case ε^{acc} is affected by fatigue and plasticity. The lower plateau reduces its length by a quantity $b\varepsilon^{pl}$ after a plastic strain equals to ε^{pl}. Parameter B regulates lower plateau stress threshold according to its length reduction, connecting them with a linear proportionality. During the B parameter calibration, also A and Φ parameters affect lower plateau position, so B value can be obtained, knowing $\Delta\sigma$ (Figure 6) from the following equation:

$$\Delta\sigma - \frac{3}{2}A\Phi\varepsilon^{acc} = B\frac{3}{2}\varepsilon^{pl} \tag{44}$$

6. Numerical tests

6.1. Description of fatigue and plasticity phenomena

In order to test the model capability to describe desired aspects of fatigue and plasticity, the proposed algorithm was implemented in the *driver code* and several loading conditions were investigated using arbitrary but reliable material

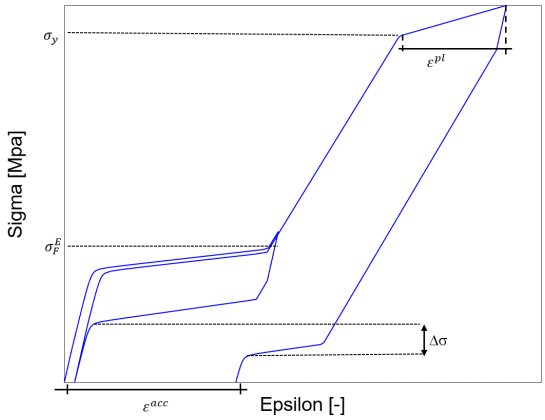

Figure 6: Stress-strain curve of an uniaxial tensile test used for B and b calibration. In the figure total accumulated strain, plastic strain and lower plateau drop due to plasticity are highlighted.

parameters (Table 4).

The two coefficients for E, h_2 and h' in Table 4 refer to high temperature ($T > A_f$) and low temperature ($T < M_f$) tests, respectively. A very high value of h_2 is required by the model to obtaine the same slope for multi-variant martensite and induced single-variant martensite.

Figure 7 reports the stress-strain curves obtaind at $T > A_f$ imposing: a) ten loading-unloading tensile cycles till 600 MPa ($< \sigma_y$); b) ten cycles in tension followed by ten cycles in compression till 600 MPa; c) one loading-unloading cycle till 1000 MPa ($> \sigma_y$). In Figures 7a and 7b fatigue effects are evident in gradual accumulation of irreversible strain and degradation of phase transformation plateaus, higher for upper plateaus than for lower one. A progressive increase in plateau slope h_1 can also be observed, determined by parameter h'. As per Barrera model, cycles in tension correctly affect cycles in compression. In Figure 7c material overcome its yielding point during loading and it recovers only partially its original shape during unloading: plasticity causes a more pronounced drop and length reduction in the lower plateau respect to the case

Table 4: Used parameters for first tests

E[MPa]	ν	h_1[MPa]	h_2[MPa]	h'[MPa]	H_1	ε_L
$50/25 \cdot 10^3$	0.35	1500	$20{\cdot}10^3/10^5$	$10^4/0$	5000	0.04
$\alpha[K^{-1}]$	T_0[K]	β[MPa/K]	M_f	A[MPa]	B[MPa]	Φ
10^{-6}	245	3	235	4000	2000	0.3
R_1[MPa]	R_2[MPa]	b	k	δ		
100	750	1	0.02	10^{-7}		

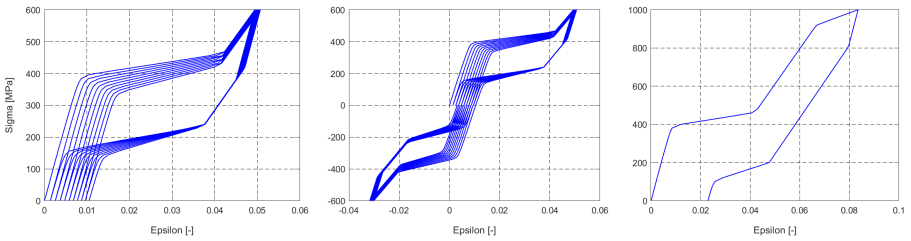

(a) (b) (c)

Figure 7: Pseudo-elastic effect. Stress-strain curves at constant temperature ($T = 310K > A_f$). a) Tensile cycles below yielding stress. b) Cycles in tension followed by cycles in compression below yielding stress. c) One tensile cycle above yielding stress.

in which only fatigue is activated (Fig. 7a): when the material overwhelms its yielding threshold the mechanical hysteresis appears with an increased height. Similar tests were performed at $T < M_f$ (Fig. 8): after each loading-unloading cycle at constant temperature, a thermal cycle is performed increasing the temperature above A_f and decrising it again below M_f to obtain the shape memory effect. Figures 8a and 8b show how during cyles the material capability of termally recovering the original shape is reduced due to fatigue. When plasticity is present (Fig. 8c) this effect is more pronounced.

For highlighting the improvements introduced by the model with respect the

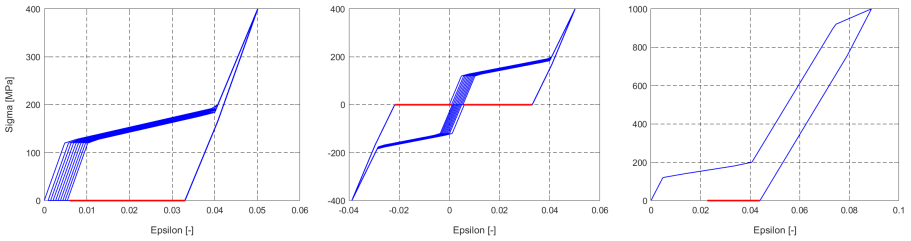

(a) (b) (c)

Figure 8: Shape memory effect. Stress-strain curves varying the temperature between $230K$ ($< M_f$), applied during each loading-unloading cycle, and $280K$ ($> A_f$), applied after unloding during stress free shape recovery. a) Tensile cycles below yielding stress; in red the partial strain recovery due to fatigue. b) Cycles in tension followed by cycles in compression below yielding stress. c) One tensile cycle above yielding stress; in red the partial strain recovery due to plasticity.

ones previously proposed by Auricchio et al. (2007) and Barrera et al. (2014), in Figure 9 are compared the results of the three tests already described: i) ten loading-unloading tensile cycles; ii) ten cycles in tension followed by ten cycles in compression; iii) one loading-unloading cycle up to yielding limit. From the plots the advantages of the new model are evident: i) it takes into account different moduli for austenite and martensite; ii) the upper and lower plateaus have a different drop during cycles; iii) during transformation phase the plateau slope may change; iv) plasticity and fatigue are described by the same model, while in Auricchio model plasticity is not described (Section 2.2) and in Biscari model plasticity and fatigue are caught if supremum norm and taxicab norm are used for defining the elastic domain limit surface, respectively (Section 2.3).

The robustness of the proposed solution algorithm was verified performing stress-controlled tests and imposing different stress increments. In Figure 10 the results of a uniaxial tensile test till 1000 MPa, using 100 MPa, 50 MPa and 25 MPa stress increments, are plotted: the model converges in all the cases, catching the same shape of stress-strain relationship.

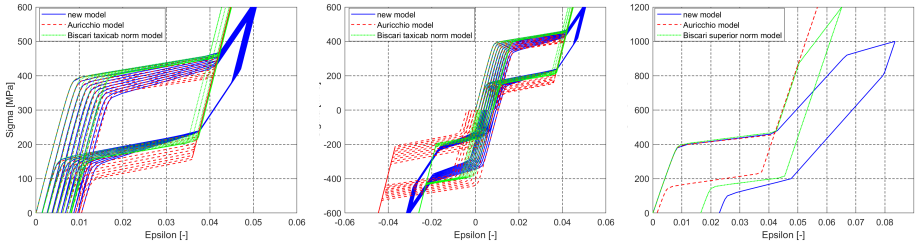

(a) (b) (c)

Figure 9: Comparison among the proposed model, Auricchio model and Biscari model. Stress-strain curves at constant temperature ($T = 310K > A_f$). a) Tensile cycles below yielding stress. b) Cycles in tension followed by cycles in compression below yielding stress. c) One tensile cycle above yielding stress.

6.2. Sensitivity analysis of model parameters

In this section we will discuss how the model parameters affect the stress-strain curves. In particular, we will refer to the pseudo-elastic behavior ($T > A_f$) and to $k, A, \Phi, h^{'}, b$ and B parameters, because h_2 was already introduced by Urbano and Auricchio (2015), H_1 has the clear meaning of controlling the slope during yielding, being the isotropic hardening coefficient, while others are the same used in the original SAP model. Parameters of Table 4 are used as starting values of cyclic tensile tests till 600 MPa. Figure 11 shows the effect of k parameter varying from 0.005 to 0.06: k is the factor controlling the transformation strain accumulation due to fatigue and its increment determines a higher residual strain at each performed cycle. It affects also degradation effect and plateau slope increase being both the phenomena proportional to the accumulated strain. Parameter A regulates the higher plateau drop during fatigue accumulation (Figure 12), while the lower plateau drop depends on the product $A \cdot \Phi$: when $\Phi = 0$ inferior plateau remains fixed, when $\Phi = 1$ both plateaus move in the same way (Figure 13). The parameter h' is responsible of progressive plateau slope increasing during fatigue. When this parameter is null at each cycle the plateaus remain parallel to the first ones; on the contrary,

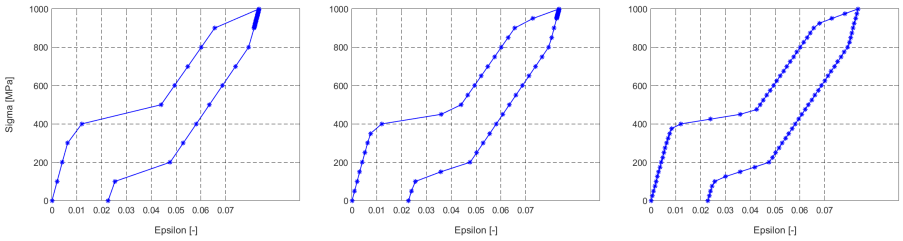

(a) (b) (c)

Figure 10: Model robustness verification. Comparison between tests with different stress increments: a) 100 MPa step; b) 50 MPa and c) 25MPa.

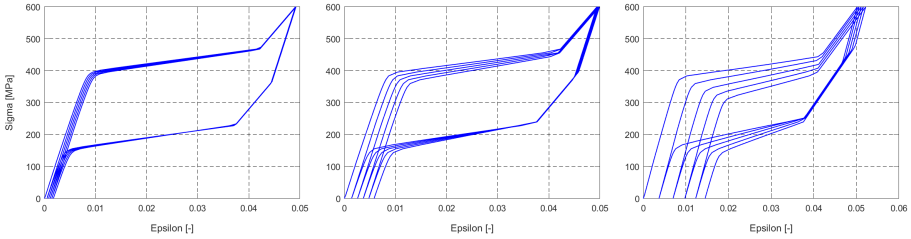

(a) (b) (c)

Figure 11: k parameter effects on stress-strain curves in a cyclic loading-unloading test till 600 MPa: a) k= 0.005; b) k= 0.02 and c) k=0.06.

increasing h' the effect on the plateau slop variation is more evident (Figure 14).

To investigate the effects of b and B, a test composed by two loading-unloading cycles, the first one till 600 MPa (no material yielding) and the second one till 1000 MPa (material plasticity) was simulated. Figure 16 shows the effect of b on lower plateau length reduction following plastic deformation: when $b = 0$ no reduction is present, and residual strain is equal to developed plastic strain (plus a small amount of strain due to fatigue); instead choosing $b = 1$ residual strain is twice the previous one, because plateau length has reduced by the quantity be^{pl}. The B parameter influences the position of the lower plateau: increasing it, the lower plateau has an evident drop, connected with a higher height of

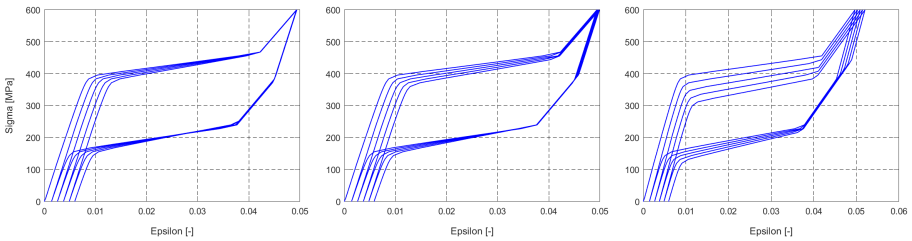

(a) (b) (c)

Figure 12: A parameter effects on stress-strain curves in a cyclic loading-unloading test till 600 MPa: a) A= 2000; b) A= 4000 and c) A=12000.

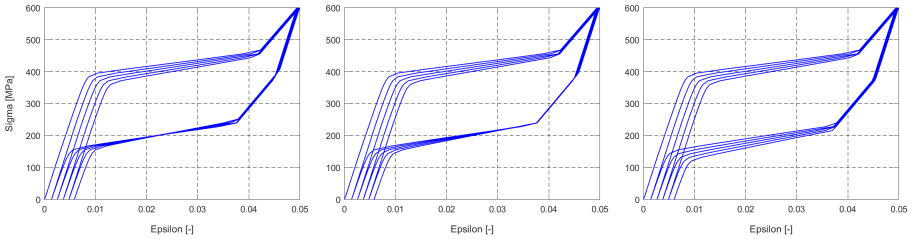

(a) (b) (c)

Figure 13: Φ parameter effects on stress-strain curves in a cyclic loading-unloading test till 600 MPa: a) $\Phi = 0$; b) $\Phi = 0.3$ and c) Φ =1.

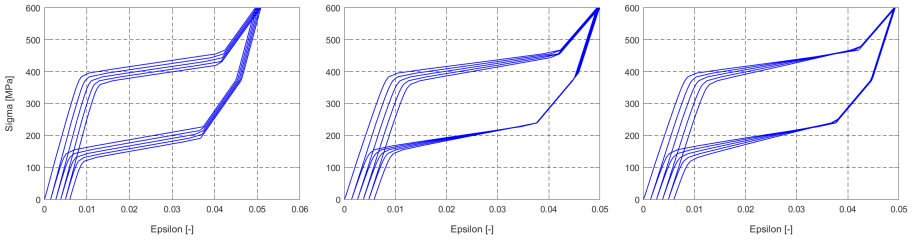

(a) (b) (c)

Figure 14: h' parameter effects on stress-strain curves in a cyclic loading-unloading test till 600 MPa: a) h'= 0; b) h'= 10000 and c) h'=20000.

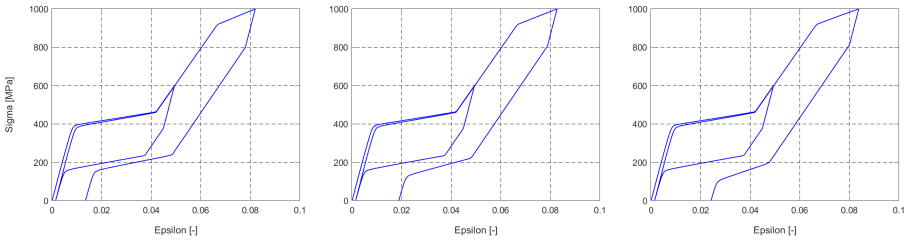

(a) (b) (c)

Figure 15: b parameter effects on stress-strain curves in a cyclic loading-unloading test till 600 MPa, followed by a second cycle till 900 MPa: a) b= 0; b) b=0.5 and c) b=1.

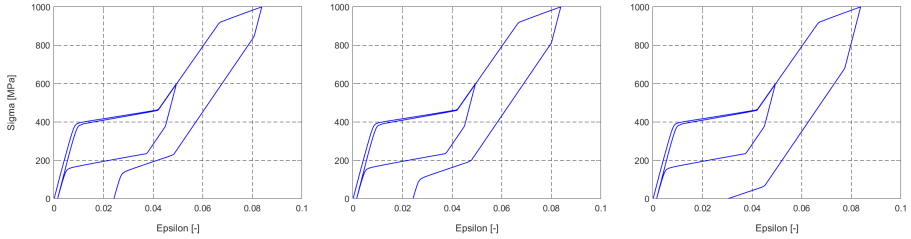

(a) (b) (c)

Figure 16: B parameter effects on stress-strain curves in a cyclic loading-unloading test till 600 MPa, followed by a second cycle till 900 MPa: a) B= 500; b) B= 2000 and c) B=10000.

hysteresis loop (Fig. 15).

6.3. Comparison with experimental results from literature

The model was also used to reproduce some experimental results published in the literature. In particular, the work of Wang et al. (2008) was taken into account: they performed a wide set of strain-driven uniaxial tensile tests up to different maximum strain (from 0.05 to 0.12) at $T = 310K$ aiming to investigate the fatigue behavior, also in presence of yielding. Not being available the experimental data, the model parameters were qualitatively estimated from an observation of the published curves. These values are summarized in Table 5,

Table 5: Used parameters for the comparison with Wang et al. (2008) experimental data

E[MPa]	ν	h_1[MPa]	h_2[MPa]	h'[MPa]	H_1	ε_L
$50{\cdot}10^3$	0.3	150	$7{\cdot}10^3$	$9{\cdot}10^3$	3000	0.063
$\alpha[K^{-1}]$	T_0[K]	β[MPa/K]	M_f	A[MPa]	B[MPa]	Φ
10^{-6}	245	3.8	235	5000	5000	0
R_1[MPa]	R_2[MPa]	b	k	δ		
100	520	1	0.03	10^{-7}		

while the comparison between experimental and model results is reported in Figure 17. From a qualitative point of view, the proposed model is able to describe experimental data, especially in case of tests at higher maximum strain, where plasticity is present.

Also the results of a stress-driven cyclic loading-unloading test performed by Kan and Kang (2010) at $T = 310K$ were simulated using the parameteres listed in Table 6, still qualitatively estimated. A good agreement between model and experimental results were found (Figure 18): the model is able to correctly catch the most important aspect of this test, i.e. the progressive movement of the curves towards higher strain values and the gradual increase in plateau slope.

7. Boudary value problems

The model was implemented in the commercial finite element code Abaqus by a UMAT user subroutine (Simulia, 2018) and used to reproduce some experimental results published in the literature where multiaxial cyclic loads were imposed to pseudo-elastic SMA Nickel-Titanium tubes (test temperature greater than A_f). In particular, the reference papers are Wang et al. (2010) and Song et al. (2014).

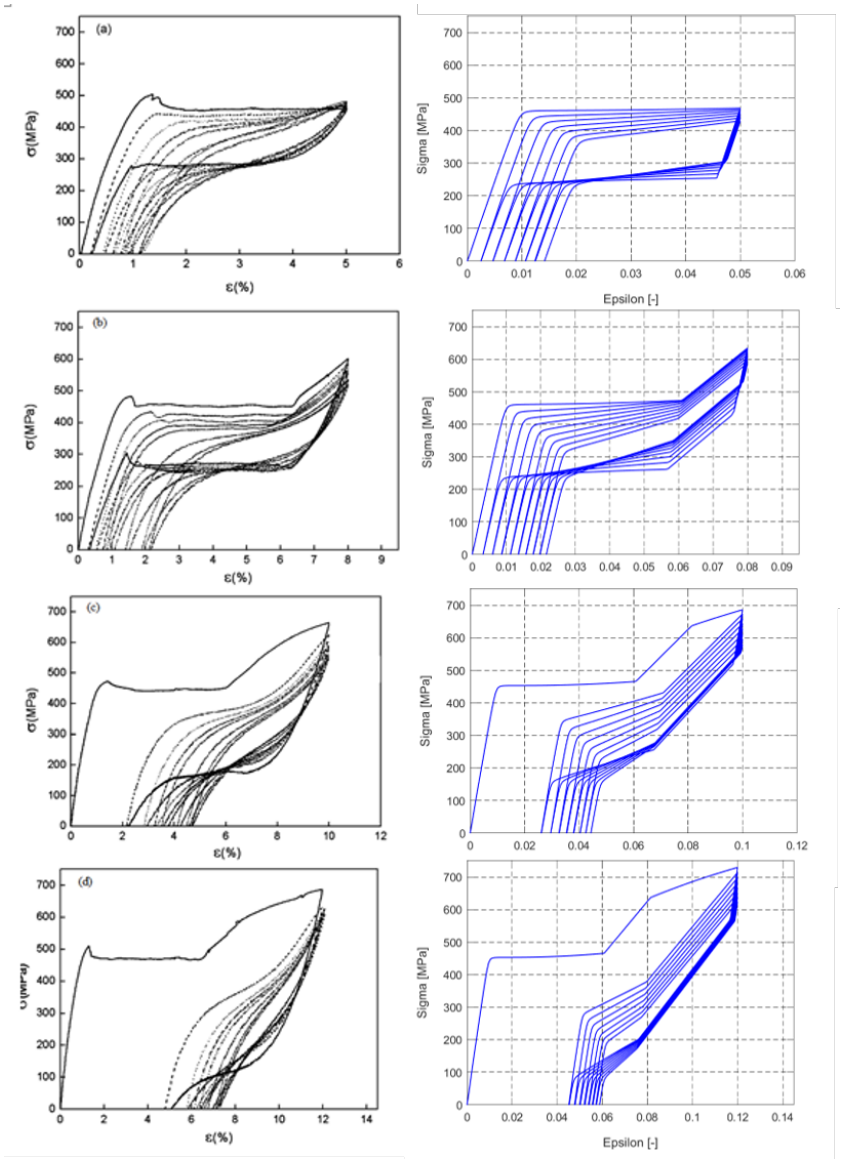

Figure 17: Comparison between stress-strain curves taken from Wang et al. (2008), on the left, with the ones obtained from the proposed model, on the right.

Table 6: Used parameters for the comparison with Kan and Kang (2010) experimental data

E[MPa]	ν	h_1[MPa]	h_2[MPa]	h'[MPa]	H_1	ε_L
$60{\cdot}10^3$	0.3	6000	–	10^6	-	0.04
$\alpha[K^{-1}]$	T_0[K]	β[MPa/K]	M_f	A[MPa]	B[MPa]	Φ
10^{-6}	245	2.8	235	8000	-	0.9
R_1[MPa]	R_2[MPa]	b	k	δ		
50	-	-	0.04	10^{-7}		

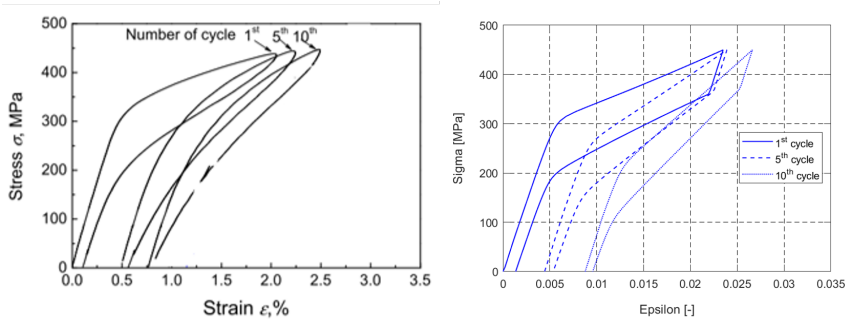

Figure 18: Comparison between stress-strain curves taken from Kan and Kang (2010), on the left, with the ones obtained from the proposed model, on the right.

In Wang et al. (2010), a specimen, having gauge length L of 24 mm, inner Φ_i and outer Φ_e diameter of 10 mm and 11.6 mm, respectively, was subjected to cyclic proportional and non-proportional tension-torsion biaxial loads at ambient temperature (T=295K $> A_f$=268K) under axial displacement and torsional angle control. The testing machine input was given according to a sine wave form such that the imposed strain path was:

$$\begin{aligned} \varepsilon(t) &= \frac{\varepsilon_{max}}{2} + \frac{\varepsilon_{max}}{2} sin(wt - 90°) \\ \gamma(t) &= \frac{\gamma_{max}}{2} + \frac{\gamma_{max}}{2} sin(wt - 90° - \phi) \end{aligned} \tag{45}$$

The recorded cross head displacement divided by the specimen gauge length

was used to calculate the nominal tensile strain, while the recorded torsional angle θ was used to calculate the shear strain, according to the formula $\gamma = (\Phi_e - \Phi_i)\theta/(4L)$. Finally, the results were reported in terms of equivalent strain and stress according to the rules:

$$\begin{aligned} \varepsilon_{eq} &= \sqrt{\varepsilon^2 + \frac{\gamma^2}{3}} \\ \sigma_{eq} &= \sqrt{\sigma^2 + 3\tau^2} \end{aligned} \tag{46}$$

In Song et al. (2014), a specimen, having gauge length L of 30 mm, inner Φ_i and outer Φ_e diameter of 1.68 mm and 2.01 mm, respectively, was subjected to cyclic proportional and non-proportional tension-torsion tests with different mutiaxial loading path and mean axial stresses. The tests were performed at ambient temperature (T=298K $> A_f$=290K) and controlled by axial load and torque moment. Also in this case, nominal tensile strain and shear strain were obtained from the recorded cross head displacement and torsional angle. Finally, the results were reported in terms of axial strain versus equivalent shear strain ($\gamma/\sqrt{3}$).

In both the papers, no information about material parameters is given. However, the authors reported also the results of cyclic tensile tests and they were used for qualitatively estimating the material model parameters. These values are summarized in Table 7, while the comparisons between experimental and model results, for the first cycles, are reported in Figures 19 and 20.

The numerical models of the two specimens were developed in the code Abaqus, according to the dimensions reported above: a kinematic coupling constraint was used to impose boundary conditions at the extremities of the models, introducing two external reference points along the tube axis. In particular, for the case of Wang et al. (2010) displacements and rotations according to the Equations 45 for the conditions ϕ=0° and ϕ=90° were applied as input and reactions in terms of cyclic axial force and torque moment were obtained as outputs. For the case of Song et al. (2014), the specimen model (Figure 21a) was loaded by axial force and torque moment according to the square and

Table 7: Used parameters for the comparison with Wang et al. (2010) (first line) and Song et al. (2014) (second line) experimental data

E[MPa]	ν	h_1[MPa]	h_2[MPa]	h'[MPa]	H_1	ε_L
$30{\cdot}10^3$	0.35	3800	10000	-	-	0.033
$47{\cdot}10^3$	0.35	1500	35000	-	-	0.05
$\alpha[K^{-1}]$	T_0[K]	β[MPa/K]	M_f	A[MPa]	B[MPa]	Φ
10^{-6}	245	5	263	9100	-	0.6
10^{-6}	245	3.7	254	14000	-	0.4
R_1[MPa]	R_2[MPa]	b	k	δ		
110	-	-	0.035	10^{-7}		
155	-	-	0.01	10^{-7}		

hourglass-typed paths plotted in Figure 21 b and c. Global displacements and rotations were obtained as outputs.

In Figures 22 and 23 the experimental data of Wang et al. (2010) and the numerical results for the first cycles of the proportional and non-proportional cases are compared in terms of tensile $\sigma-\varepsilon$ curves (a), shear $\sqrt{3}\tau-\gamma/\sqrt{3}$ curves (b) and equivalent stress-strain curves (c), while in Figure 24 the comparison with the data published by Song et al. (2014) for the square path (top) and hourglass path (bottom) is displayed in terms of axial strain - equivalent shear strain.

The results show a quite good capabilty of the model to catch, at least from a qualitative point of view, the SMA cyclic behaviour also under complex loading paths. Clearly, for a better validation of the model it would be necessary to have all the information useful for a correct and complete calibration of the material model parameters.

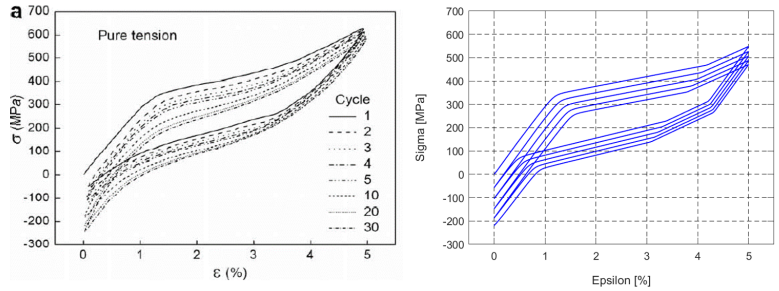

Figure 19: Comparison between uniaxial stress-strain curves reported in Wang et al. (2010), on the left, with the first five cycles obtained by the proposed model, on the right.

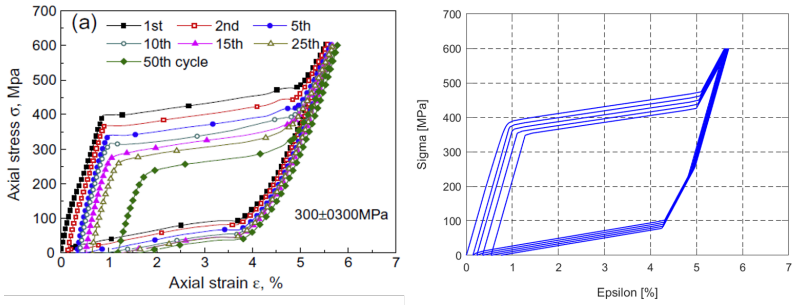

Figure 20: Comparison between uniaxial stress-strain curves reported in Song et al. (2014), on the left, with the first five cycles obtained by the proposed model, on the right.

8. Conclusions

In this paper a further development of the 3D phenomenological model initally proposed by Souza et al. (1998) and Auricchio and Petrini (2004), and revised by Auricchio et al. (2007) and Barrera et al. (2014), is presented. The added improvements allow to catch the most significant effects of functional fatigue and plasticity on the SMA super-elastic behavior, as shown also by the comparison with some uniaxial experimental tests. Several numerical tests were perfomed highlighting the model response during uniaxial cyclic loading. In detail, when cyclic loads are applied below yielding stress, the model is able to take into account the increment of inelastic strains, the different drop of the trans-

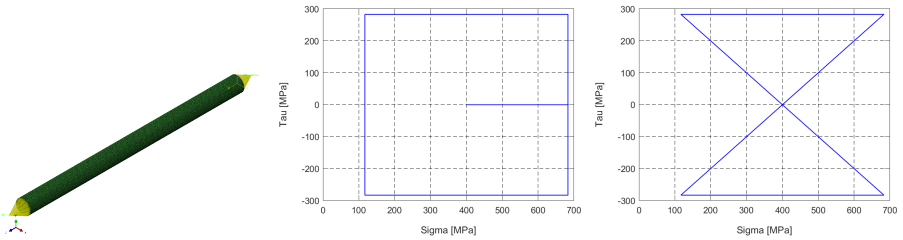

(a) (b) (c)

Figure 21: Numerical simulation of the tests performed by Song et al. (2014). a) Model of the specimen: the length is assumed equal to the gauge length and kinematic coupling constraints are imposed to the two extremities through the indicated reference points. b) Square and c) hourglass-typed loading paths imposed to the specimen.

formation plateaus and their slope change, the reduction of the transformation domain. When yielding is overcome, the model catches the influence of plastic strain on the material shape recovery capability and on the transformation hysteresis dimension. Moreover, the model implementation in a commercial finite element code allowed to simulate also some proportional and non-proportional biaxial experimental tests, published in the literature, showing its ability to describe very different loading conditions.

The model is also able to describe the shape memory effect, however its capability to correctly catch the effects of fatigue and plasticty during thermomechanical cycles has to be still investigated through ad hoc comparisons with experimental results.

The model depends on a limitated number of parameters, with a clear physical meaning and easily to be evaluated by few uniaxial experimental tests. Finally, some limitations are presents: the asymmetric behavior in tension and compression is disregarded, the inelastic strain accumulation is constant, fatigue and plasticity are coupled above yielding. Their overcoming will be object of feature studies.

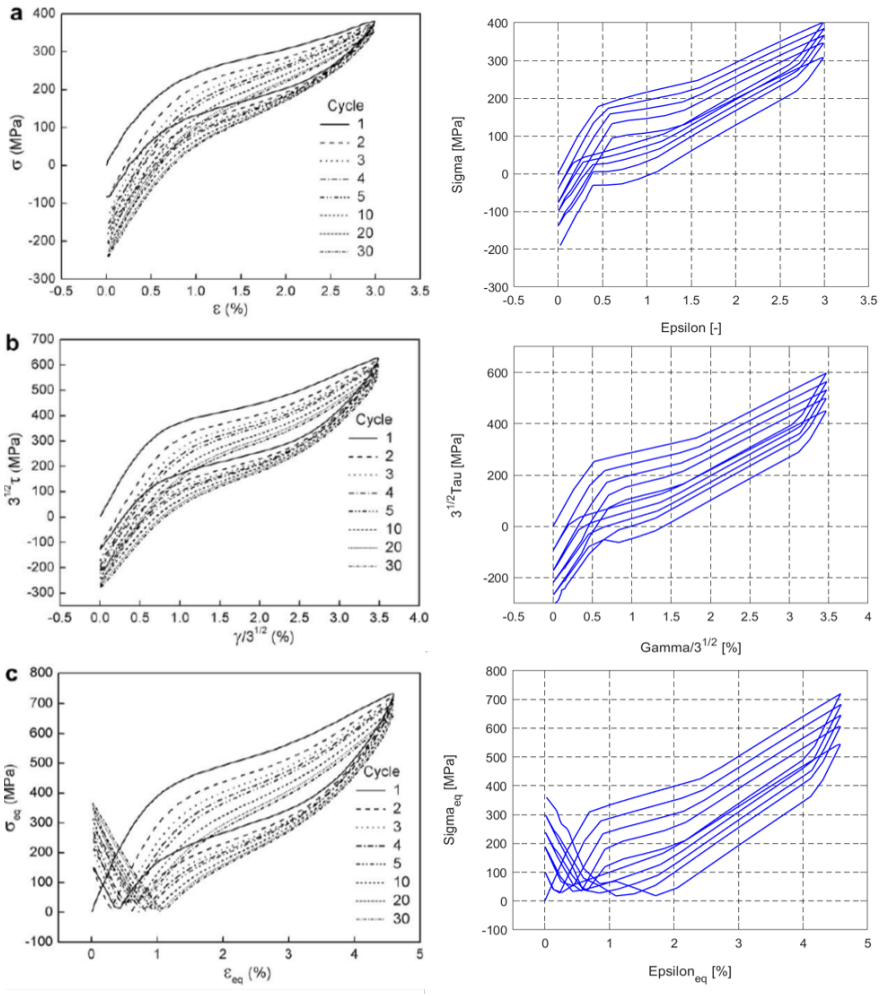

Figure 22: Comparison between proportional (input signals are in phase) stress-strain curves taken from Wang et al. (2010), on the left, with the one obtained from the proposed model, on the right: a) axial stress-strain curves, (b) shear stress-strain curves, (c) equivalent stress-strain curves.

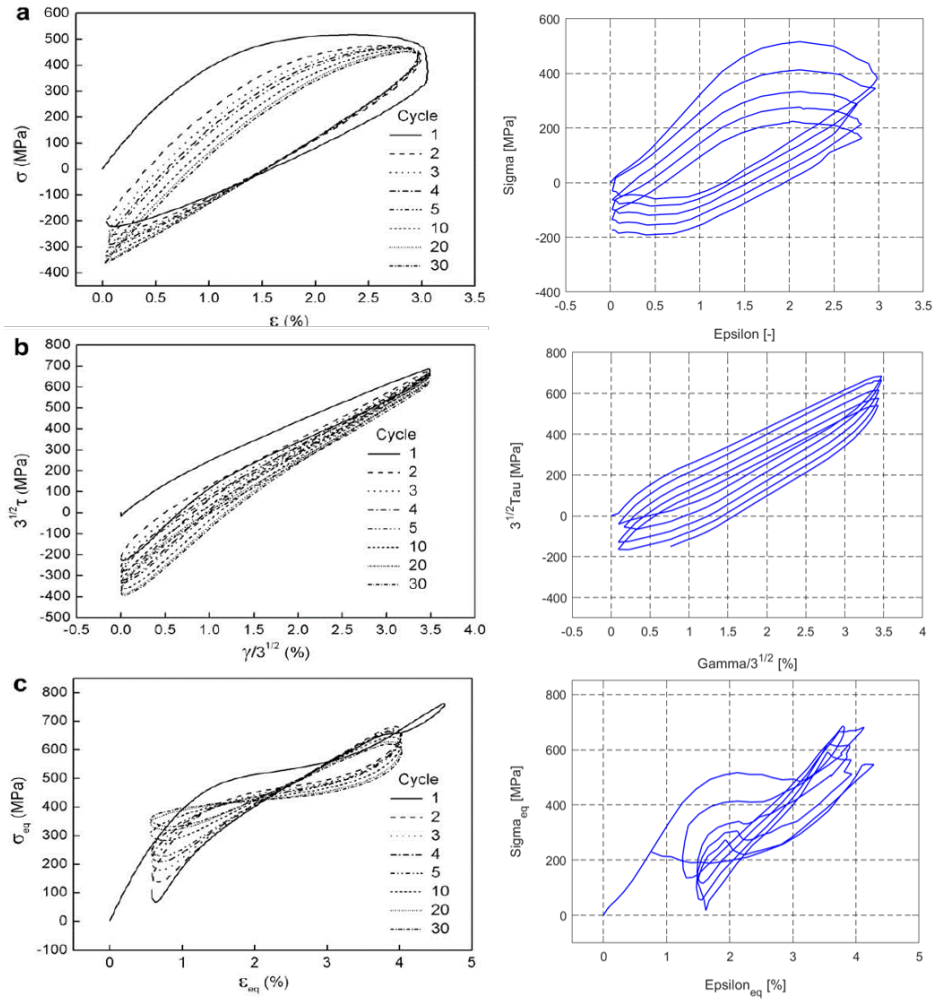

Figure 23: Comparison between non proportional (input signals are 90° out of phase) stress-strain curves taken from Wang et al. (2010), on the left, with the ones obtained from the proposed model, on the right: a) axial stress-strain curves, (b) shear stress-strain curves, (c) equivalent stress-strain curves.

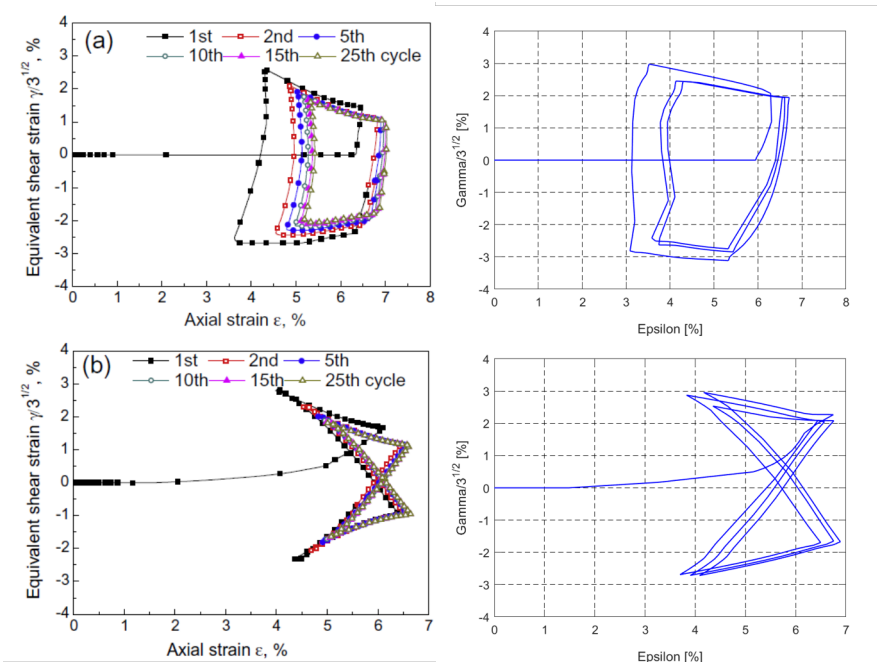

Figure 24: Comparison between stress-strain curves taken from Song et al. (2014), on the left, with the ones obtained from the proposed model, for the square (top) and the hourglass-typed (bottom) loading paths.

Acknowledgments

The authors would like to thank Prof. Paolo Biscari, from Politecnico di Milano, and Prof. Ulisse Stefanelli, from University of Vienna, for the useful discussions about the modeling strategy, Dr. Francesca Berti, from Politecnico di Milano, for her help in numerical simulations.

References

Arghavani, J., Auricchio, F., Naghdabadi, R., Reali, A., 2011. An improved, fully symmetric, finite-strain phenomenological constitutive model for shape memory alloys. Finite Elements in Analysis and Design 47, 166–174. URL: http://dx.doi.org/10.1016/j.finel.2010.09.001, doi:10.1016/j.finel.2010.09.001.

Auricchio, F., Petrini, L., 2004. A three-dimensional model describing stress-temperature induced solid phase transformations: solution algorithm and boundary value problems. International Journal for Numerical Methods in Engineering 61, 807–836. URL: http://dx.doi.org/10.1002/nme.1086, doi:10.1002/nme.1086.

Auricchio, F., Reali, A., Stefanelli, U., 2007. A three-dimensional model describing stress-induced solid phase transformation with permanent inelasticity. International Journal of Plasticity 23, 207 – 226. URL: http://www.sciencedirect.com/science/article/pii/S0749641906000714, doi:https://doi.org/10.1016/j.ijplas.2006.02.012.

Auricchio, F., Taylor, R.L., 1997. Shape-memory alloys: modelling and numerical simulations of the finite-strain superelastic behavior. Computer Methods in Applied Mechanics and Engineering 143, 175 – 194. URL: http://www.sciencedirect.com/science/article/pii/S0045782596011474, doi:https://doi.org/10.1016/S0045-7825(96)01147-4.

Barrera, N., Biscari, P., Urbano, M.F., 2014. Macroscopic modeling of functional fatigue in shape memory alloys. European Journal of Mechanics - A/Solids 45, 101 – 109. URL: http://www.sciencedirect.com/science/article/pii/S0997753813001502, doi:https://doi.org/10.1016/j.euromechsol.2013.11.015.

Bouvet, C., Calloch, S., Lexcellent, C., 2004. A phenomenological model for pseudoelasticity of shape memory alloys under multiaxial proportional and nonproportional loadings. European Journal of Mechanics - A/Solids 23, 37 – 61. URL: http://www.sciencedirect.com/science/article/pii/S0997753803001104, doi:https://doi.org/10.1016/j.euromechsol.2003.09.005.

Brinson, L., Schmidt, I., Lammering, R., 2004. Stress-induced transformation behavior of a polycrystalline niti shape memory alloy: micro and macromechanical investigations via in situ optical microscopy. Journal of the Mechanics and Physics of Solids 52, 1549 – 1571. URL: http://www.sciencedirect.com/science/article/pii/S0022509604000079, doi:https://doi.org/10.1016/j.jmps.2004.01.001.

Chatziathanasiou, D., Chemisky, Y., Chatzigeorgiou, G., Meraghni, F., 2016. Modeling of coupled phase transformation and reorientation in shape memory alloys under non-proportional thermomechanical loading. International Journal of Plasticity 82, 192–224. URL: http://dx.doi.org/10.1016/j.ijplas.2016.03.005, doi:10.1016/j.ijplas.2016.03.005.

Chemisky, Y., Chatzigeorgiou, G., Kumar, P., Lagoudas, D.C., 2014. Mechanics of Materials A constitutive model for cyclic actuation of high-temperature shape memory alloys. Mechanics of Materials 68, 120–136. URL: http://dx.doi.org/10.1016/j.mechmat.2013.07.020, doi:10.1016/j.mechmat.2013.07.020.

Christ, D., Reese, S., 2008. Finite-element modelling of shape memory alloysa comparison between small-strain and large-strain for-

mulations. Materials Science and Engineering: A 481-482, 343 – 346. URL: http://www.sciencedirect.com/science/article/pii/S0921509307011914, doi:https://doi.org/10.1016/j.msea.2006.11.174. proceedings of the 7th European Symposium on Martensitic Transformations, ESOMAT 2006.

Christ, D., Reese, S., 2009. A finite element model for shape memory alloys considering thermomechanical couplings at large strains. International Journal of Solids and Structures 46, 3694–3709. URL: http://dx.doi.org/10.1016/j.ijsolstr.2009.06.017, doi:10.1016/j.ijsolstr.2009.06.017, arXiv:arXiv:1006.4405v1.

Cisse, C., Zaki, W., Zineb, T.B., 2016a. A review of constitutive models and modeling techniques for shape memory alloys. International Journal of Plasticity 76, 244 – 284. URL: http://www.sciencedirect.com/science/article/pii/S0749641915001436, doi:https://doi.org/10.1016/j.ijplas.2015.08.006.

Cisse, C., Zaki, W., Zineb, T.B., 2016b. A review of modeling techniques for advanced effects in shape memory alloy behavior. Smart Materials and Structures 25, 103001. URL: http://stacks.iop.org/0964-1726/25/i=10/a=103001.

Darren J. Hartl, D.C.L., 2008. Simultaneous transformation and plastic deformation in shape memory alloys. Proc. SPIE Behavior and Mechanics of Multifunctional and Composite Materials 2008 6929, 1 – 10. URL: http://dx.doi.org/10.1117/12.776583, doi:10.1117/12.776583.

Delville, R., Malard, B., Pilch, J., Sittner, P., Schryvers, D., 2011. Transmission electron microscopy investigation of dislocation slip during superelastic cycling of niti wires. International Journal of Plasticity 27, 282 – 297. URL: http://www.sciencedirect.com/science/article/pii/S0749641910000707, doi:https://doi.org/10.1016/j.ijplas.2010.05.005.

Duerig, T., Melton, K., Stockel, D., Wayman, C., 1990. Engineering Aspects of Shape Memory Alloys. Butterworth-Heinemann Ltd.

Eggeler, G., Hornbogen, E., Yawny, A., Heckmann, A., Wagner, M., 2004. Structural and functional fatigue of niti shape memory alloys. Materials Science and Engineering: A 378, 24 – 33. URL: http://www.sciencedirect.com/science/article/pii/S0921509303015144, doi:https://doi.org/10.1016/j.msea.2003.10.327. european Symposium on Martensitic Transformation and Shape-Memory.

Falk, F., 1983. One-dimensional model of shape memory alloys. Archives of Mechanics 35, 63 – 84.

Gall, K., Maier, H., 2002. Cyclic deformation mechanisms in precipitated niti shape memory alloys. Acta Materialia 50, 4643 – 4657. URL: http://www.sciencedirect.com/science/article/pii/S1359645402003154, doi:https://doi.org/10.1016/S1359-6454(02)00315-4.

Gall, K., Sehitoglu, H., Anderson, R., Karaman, I., Chumlyakov, Y.I., Kireeva, I.V., 2001. On the mechanical behavior of single crystal niti shape memory alloys and related polycrystalline phenomenon. Materials Science and Engineering: A 317, 85 – 92. URL: http://www.sciencedirect.com/science/article/pii/S0921509301011832, doi:https://doi.org/10.1016/S0921-5093(01)01183-2.

Hartl, D.J., Chatzigeorgiou, G., Lagoudas, D.C., 2010. Three-dimensional modeling and numerical analysis of rate-dependent irrecoverable deformation in shape memory alloys. International Journal of Plasticity 26, 1485–1507. URL: http://dx.doi.org/10.1016/j.ijplas.2010.01.002, doi:10.1016/j.ijplas.2010.01.002.

Hartl, D.J., Lagoudas, D.C., 2009. Constitutive modeling and structural analysis considering simultaneous phase transformation and plastic yield in

shape memory alloys. Smart Materials and Structures 18, 104017. URL: http://stacks.iop.org/0964-1726/18/i=10/a=104017.

Kan, Q., Kang, G., 2010. Constitutive model for uniaxial transformation ratchetting of super-elastic niti shape memory alloy at room temperature. International Journal of Plasticity 26, 441 – 465. URL: http://www.sciencedirect.com/science/article/pii/S0749641909000990, doi:https://doi.org/10.1016/j.ijplas.2009.08.005.

Kan, Q., Yu, C., Kang, G., Li, J., Yan, W., 2016. Experimental observations on rate-dependent cyclic deformation of super-elastic NiTi shape memory alloy. Mechanics of Materials 97, 48–58. URL: http://dx.doi.org/10.1016/j.mechmat.2016.02.011, doi:10.1016/j.mechmat.2016.02.011.

Kang, G., Kan, Q., Qian, L., Liu, Y., 2009. Ratchetting deformation of super-elastic and shape-memory niti alloys. Mechanics of Materials 41, 139 – 153. URL: http://www.sciencedirect.com/science/article/pii/S0167663608001191, doi:https://doi.org/10.1016/j.mechmat.2008.09.001.

Kang, G., Kan, Q., Yu, C., Song, D., Liu, Y., 2012. Whole-life transformation ratchetting and fatigue of super-elastic niti alloy under uniaxial stress-controlled cyclic loading. Materials Science and Engineering: A 535, 228 – 234. URL: http://www.sciencedirect.com/science/article/pii/S0921509311014523, doi:https://doi.org/10.1016/j.msea.2011.12.071.

Khandelwal, A., Buravalla, V., 2009. Models for shape memory alloy behavior: An overview of modeling approaches. International Journal of Structural Changes in Solids 1, 118 – 148. URL: http://stacks.iop.org/0964-1726/25/i=10/a=103001.

Lagoudas, C., Entchev, P., 2004. Modeling of transformation-induced plasticity and its effect on the behavior of porous shape memory alloys. part i: con-

stitutive model for fully dense smas. Mechanics of Material 36, 865–892. doi:10.1016/j.mechmat.2003.08.006.

Lagoudas, D., Hartl, D., Chemisky, Y., MacHado, L., Popov, P., 2012. Constitutive model for the numerical analysis of phase transformation in polycrystalline shape memory alloys. International Journal of Plasticity 32-33, 155–183. URL: http://dx.doi.org/10.1016/j.ijplas.2011.10.009, doi:10.1016/j.ijplas.2011.10.009.

Lagoudas, D.C., Entchev, P.B., Popov, P., Patoor, E., Brinson, L.C., Gao, X., 2006. Shape memory alloys, part ii: Modeling of polycrystals. Mechanics of Materials 38, 430 – 462. URL: http://www.sciencedirect.com/science/article/pii/S0167663605001201, doi:https://doi.org/10.1016/j.mechmat.2005.08.003. shape Memory Alloys.

Lecce, L., Concolio, L. (Eds.), 2014. Shape Memory Alloy Engineering for Aerospace, Structural and Biomedical Applications. Butterworth-Heinemann Ltd.

Lemaitre, J., Chaboche, J.L., 1990. Mechanics of Solid Materials. Cambridge University Press. doi:10.1017/CBO9781139167970.

Li, Y., Mi, X., Tan, J., Gao, B., 2009. Thermo-mechanical cyclic transformation behavior of tini shape memory alloy wire. Materials Science and Engineering: A 509, 8 – 13. URL: http://www.sciencedirect.com/science/article/pii/S0921509309001968, doi:https://doi.org/10.1016/j.msea.2009.02.041.

Lim, T.J., McDowell, D.L., 1999. Mechanical behavior of an ni-ti shape memory alloy under axial-torsional proportional and nonproportional loading. ASME, Journal of Engineering Materials and Technology 121, 9 – 18. doi:10.1115/1.2816007.

Malagisi, S., Marfia, S., Sacco, E., 2017. Coupled normal-shear stress models for sma response. Computers & Structures 193, 73 – 86. URL: http://www.sciencedirect.com/science/article/pii/S0045794917301670, doi:https://doi.org/10.1016/j.compstruc.2017.08.001.

Mammano, G.S., Dragoni, E., 2014. Functional fatigue of niti shape memory wires under various loading conditions. International Journal of Fatigue 69, 71 – 83. URL: http://www.sciencedirect.com/science/article/pii/S0142112312000874, doi:https://doi.org/10.1016/j.ijfatigue.2012.03.004. special Issue: Theory and experiments in fatigue lifetime assessment.

MATLAB, 2016. version 9.0 (R2016a). The MathWorks Inc., Natick, Massachusetts.

Melton, K., Mercier, O., 1979. Fatigue of niti thermoelastic martensites. Acta Metallurgica 27, 137 – 144. URL: http://www.sciencedirect.com/science/article/pii/0001616079900658, doi:https://doi.org/10.1016/0001-6160(79)90065-8.

Miller, D., Lagoudas, D., 2000. Thermo-mechanical characterization of niticu and niti sma actuators: inuence of plastic strains. Smart Materials and Structures 5, 640 – 652.

Miyazaki, S., Imai, T., Igo, Y., Otsuka, K., 1986. Effect of cyclic deformation on the pseudoelasticity characteristics of ti-ni alloys. Metallurgical Transactions A 17, 115–120. URL: https://doi.org/10.1007/BF02644447, doi:10.1007/BF02644447.

Mohd Jani, J., Leary, M., Subic, A., Gibson, M., 2014. A review of shape memory alloy research, applications and opportunities. Materials and Design 56, 1078–1113. doi:10.1016/j.matdes.2013.11.084.

Morgan, N., Friend, C., 2001. A review of shape memory stability in niti alloys. J. Phys. IV France 11, 325 – 332. doi:10.1051/jp4:2001855.

Morin, C., Moumni, Z., Zaki, W., 2011a. A constitutive model for shape memory alloys accounting for thermomechanical coupling. International Journal of Plasticity 27, 748 – 767. URL: http://www.sciencedirect.com/science/article/pii/S0749641910001312, doi:https://doi.org/10.1016/j.ijplas.2010.09.005.

Morin, C., Moumni, Z., Zaki, W., 2011b. Thermomechanical coupling in shape memory alloys under cyclic loadings: Experimental analysis and constitutive modeling. International Journal of Plasticity 27, 1959 – 1980. URL: http://www.sciencedirect.com/science/article/pii/S0749641911000817, doi:https://doi.org/10.1016/j.ijplas.2011.05.005. special Issue in Honor of Nobutada Ohno.

Müller, I., Wilmanski, K., 1980. A model for phase transition in pseudoelastic bodies. Il Nuovo Cimento B (1971-1996) 57, 283–318. URL: https://doi.org/10.1007/BF02729036, doi:10.1007/BF02729036.

Nemat-Nasser, S., Guo, W.G., 2006. Superelastic and cyclic response of niti sma at various strain rates and temperatures. Mechanics of Materials 38, 463 – 474. URL: http://www.sciencedirect.com/science/article/pii/S0167663605001213, doi:https://doi.org/10.1016/j.mechmat.2005.07.004. shape Memory Alloys.

Orgéas, L., Favier, D., 1998. Stress-induced martensitic transformation of a niti alloy in isothermal shear, tension and compression. Acta Materialia 46, 5579 – 5591. URL: http://www.sciencedirect.com/science/article/pii/S1359645498001670, doi:https://doi.org/10.1016/S1359-6454(98)00167-0.

Otsuka, K., Wayman, C., 1998. Shape Memory Materials. Cambridge University Press.

Paiva, A., Savi, M.A., Braga, A.M.B., Pacheco, P.M.C.L., 2005. A constitutive model for shape memory alloys considering ten-

silecompressive asymmetry and plasticity. International Journal of Solids and Structures 42, 3439 – 3457. URL: http://www.sciencedirect.com/science/article/pii/S0020768304006250, doi:https://doi.org/10.1016/j.ijsolstr.2004.11.006.

Patoor, E., Lagoudas, D.C., Entchev, P.B., Brinson, L.C., Gao, X., 2006. Shape memory alloys, part i: General properties and modeling of single crystals. Mechanics of Materials 38, 391 – 429. URL: http://www.sciencedirect.com/science/article/pii/S0167663605001195, doi:https://doi.org/10.1016/j.mechmat.2005.05.027. shape Memory Alloys.

Petrini, L., Migliavacca, F., 2011. Biomedical applications of shape memory alloys. Journal of Metallurgy , 1–15doi:10.1155/2011/5014832.

Rebelo, N., Zipse, A., Schlun, M., Dreher, G., 2011. A material model for the cyclic behavior of nitinol. Journal of Materials Engineering and Performance 20, 605–612. URL: https://doi.org/10.1007/s11665-011-9883-6, doi:10.1007/s11665-011-9883-6.

Reedlunn, B., Churchill, C.B., Nelson, E.E., Shaw, J.A., Daly, S.H., 2014. Tension, compression, and bending of superelastic shape memory alloy tubes. Journal of the Mechanics and Physics of Solids 63, 506 – 537. URL: http://www.sciencedirect.com/science/article/pii/S0022509613000082, doi:https://doi.org/10.1016/j.jmps.2012.12.012.

Reese, S., Christ, D., 2008. Finite deformation pseudo-elasticity of shape memory alloys - Constitutive modelling and finite element implementation. International Journal of Plasticity 24, 455–482. doi:10.1016/j.ijplas.2007.05.005.

Saint-Sulpice, L., Chirani, S.A., Calloch, S., 2009. A 3d superelastic model for shape memory alloys taking into account progressive strain under cyclic loadings. Mechanics of Materials 41, 12

– 26. URL: http://www.sciencedirect.com/science/article/pii/S0167663608001051, doi:https://doi.org/10.1016/j.mechmat.2008.07.004.

Sakhaei, A.H., Thamburaja, P., 2017. A finite-deformation-based constitutive model for high-temperature shape-memory alloys. Mechanics of Materials 109, 114 – 134. URL: http://www.sciencedirect.com/science/article/pii/S0167663617301801, doi:https://doi.org/10.1016/j.mechmat.2017.03.004.

Saleeb, A., Padula, S., Kumar, A., 2011. A multi-axial, multi-mechanism based constitutive model for the comprehensive representation of the evolutionary response of smas under general thermomechanical loading conditions. International Journal of Plasticity 27, 655 – 687. URL: http://www.sciencedirect.com/science/article/pii/S0749641910001178, doi:https://doi.org/10.1016/j.ijplas.2010.08.012.

Sedlák, P., Frost, M., Benesová, B., Zineb, T.B., Sittner, P., 2012. Thermomechanical model for niti-based shape memory alloys including r-phase and material anisotropy under multi-axial loadings. International Journal of Plasticity 39, 132 – 151. URL: http://www.sciencedirect.com/science/article/pii/S0749641912001027, doi:https://doi.org/10.1016/j.ijplas.2012.06.008.

Sedmak, P., Sittner, P., Pilch, J., Curfs, C., 2015. Instability of cyclic superelastic deformation of niti investigated by synchrotron x-ray diffraction. Acta Materialia 94, 257 – 270. URL: http://www.sciencedirect.com/science/article/pii/S1359645415002918, doi:https://doi.org/10.1016/j.actamat.2015.04.039.

Sehitoglu, H., Jun, J., Zhang, X., Karaman, I., Chumlyakov, Y., Maier, H., Gall, K., 2001. Shape memory and pseudoelastic behavior of 51.5%niti single crystals in solutionized and overaged state. Acta Materialia 49,

3609 – 3620. URL: http://www.sciencedirect.com/science/article/pii/S1359645401002166, doi:https://doi.org/10.1016/S1359-6454(01)00216-6.

Simulia, 2018. Abaqus Unified FEA. Dassault Systmes, Johnston, Rhode Island, United States.

Šittner, P., Lukáš, P., Novák, V., Daymond, M., Swallowe, G., 2004. In situ neutron diffraction studies of martensitic transformations in niti polycrystals under tension and compression stress. Materials Science and Engineering: A 378, 97 – 104. URL: http://www.sciencedirect.com/science/article/pii/S0921509303015259, doi:https://doi.org/10.1016/j.msea.2003.09.112. european Symposium on Martensitic Transformation and Shape-Memory.

Song, D., Kang, G., Kan, Q., Yu, C., Zhang, C., 2014. Non-proportional multiaxial transformation ratchetting of super-elastic niti shape memory alloy: Experimental observations. Mechanics of Materials 70, 94 – 105. URL: http://www.sciencedirect.com/science/article/pii/S0167663613002548, doi:https://doi.org/10.1016/j.mechmat.2013.12.003.

Souza, A.C., Mamiya, E.N., Zouain, N., 1998. Three-dimensional model for solids undergoing stress-induced phase transformations. European Journal of Mechanics - A/Solids 17, 789 – 806. URL: http://www.sciencedirect.com/science/article/pii/S0997753898800053, doi:https://doi.org/10.1016/S0997-7538(98)80005-3.

Srinivasan, A., McFarland, D., 2001. Smart Structures: Analysis and Design. Cambridge University Press, Cambridge.

Stachowiak, G., McCormick, P., 1988. Shape memory behaviour associated with the r and martensitic transformations in a niti alloy. Acta Metallurgica 36, 291 – 297. URL: http://www.sciencedirect.com/science/article/pii/0001616088900065, doi:https://doi.org/10.1016/0001-6160(88)90006-5.

Stupkiewicz, S., Petryk, H., 2013. A robust model of pseudoelasticity in shape memory alloys. International Journal for Numerical Methods in Engineering 93, 747–769. URL: http://dx.doi.org/10.1002/nme.4405, doi:10.1002/nme.4405.

Tanaka, K., Kobayashi, S., Sato, Y., 1986. Thermomechanics of transformation pseudoelasticity and shape memory effect in alloys. International Journal of Plasticity 2, 59 – 72. URL: http://www.sciencedirect.com/science/article/pii/0749641986900161, doi:https://doi.org/10.1016/0749-6419(86)90016-1.

Tanaka, K., Nishimura, F., Hayashi, T., Tobushi, H., Lexcellent, C., 1995. Phenomenological analysis on subloops and cyclic behavior in shape memory alloys under mechanical and/or thermal loads. Mechanics of Materials 19, 281 – 292. URL: http://www.sciencedirect.com/science/article/pii/016766369400038I, doi:https://doi.org/10.1016/0167-6636(94)00038-I.

Teeriaho, J.P., 2013. An extension of a shape memory alloy model for large deformations based on an exactly integrable eulerian rate formulation with changing elastic properties. International Journal of Plasticity 43, 153 – 176. URL: http://www.sciencedirect.com/science/article/pii/S0749641912001805, doi:https://doi.org/10.1016/j.ijplas.2012.11.009.

Thamburaja, P., 2005. Constitutive equations for martensitic reorientation and detwinning in shape-memory alloys. Journal of the Mechanics and Physics of Solids 53, 825 – 856. URL: http://www.sciencedirect.com/science/article/pii/S0022509604001930, doi:https://doi.org/10.1016/j.jmps.2004.11.004.

Thamburaja, P., 2010. A finite-deformation-based phenomenological theory for shape-memory alloys. International Journal of Plasticity 26, 1195–1219.

URL: http://dx.doi.org/10.1016/j.ijplas.2009.12.004, doi:10.1016/j.ijplas.2009.12.004.

Urbano, M.F., Auricchio, F., 2015. Modeling permanent deformations of superelastic and shape memory materials. Journal of Functional Biomaterials 6, 398–406. doi:doi:10.3390/jfb6020398.

Wang, X., Wang, Y., Lu, Z., Deng, C., Yue, Z., 2010. An experimental study of the superelastic behavior in niti shape memory alloys under biaxial proportional and non-proportional cyclic loadings. Mechanics of Materials 42, 365 – 373. URL: http://www.sciencedirect.com/science/article/pii/S0167663609001975, doi:https://doi.org/10.1016/j.mechmat.2009.11.010.

Wang, X., Xu, B., Yue, Z., 2008. Phase transformation behavior of pseudoelastic niti shape memory alloys under large strain. Journal of Alloys and Compounds 463, 417 – 422. URL: http://www.sciencedirect.com/science/article/pii/S0925838807017902, doi:https://doi.org/10.1016/j.jallcom.2007.09.029.

Yan, W., Wang, C.H., Zhang, X.P., Mai, Y.W., 2003. Theoretical modelling of the effect of plasticity on reverse transformation in superelastic shape memory alloys. Materials Science and Engineering: A 354, 146 – 157. URL: http://www.sciencedirect.com/science/article/pii/S0921509302009413, doi:https://doi.org/10.1016/S0921-5093(02)00941-3.

Yoneyama, T., Miyazaki, S. (Eds.), 2009. Shape Memory Alloys for Biomedical Applications. Woodhead Publishing Ltd.

Yu, C., Kang, G., Kan, Q., 2014. A physical mechanism based constitutive model for temperature-dependent transformation ratchetting of NiTi shape memory alloy: One-dimensional model. Mechanics of Materials 78, 1–10. URL: http://dx.doi.org/10.1016/j.mechmat.2014.07.011, doi:10.1016/j.mechmat.2014.07.011.

Yu, C., Kang, G., Kan, Q., Xu, X., 2017. Physical mechanism based crystal plasticity model of NiTi shape memory alloys addressing the thermo-mechanical cyclic degeneration of shape memory effect. Mechanics of Materials 112, 1–17. URL: http://dx.doi.org/10.1016/j.mechmat.2017.05.005, doi:10.1016/j.mechmat.2017.05.005.

Yu, C., Kang, G., Kan, Q., Zhu, Y., 2015. Rate-dependent cyclic deformation of super-elastic NiTi shape memory alloy: Thermo-mechanical coupled and physical mechanism-based constitutive model. International Journal of Plasticity 72, 60–90. URL: http://dx.doi.org/10.1016/j.ijplas.2015.05.011, doi:10.1016/j.ijplas.2015.05.011.

Zaki, W., 2012. An efficient implementation for a model of martensite reorientation in martensitic shape memory alloys under multiaxial nonproportional loading. International Journal of Plasticity 37, 72–94. URL: http://dx.doi.org/10.1016/j.ijplas.2012.04.002, doi:10.1016/j.ijplas.2012.04.002.

Zaki, W., Moumni, Z., 2007. A 3d model of the cyclic thermomechanical behavior of shape memory alloys. Journal of the Mechanics and Physics of Solids 55, 2427 – 2454. URL: http://www.sciencedirect.com/science/article/pii/S0022509607000750, doi:https://doi.org/10.1016/j.jmps.2007.03.011.

Zaki, W., Zamfir, S., Moumni, Z., 2010. An extension of the zm model for shape memory alloys accounting for plastic deformation. Mechanics of Materials 42, 266 – 274. URL: http://www.sciencedirect.com/science/article/pii/S0167663609002002, doi:https://doi.org/10.1016/j.mechmat.2009.11.013.

Zhou, B., 2012. A macroscopic constitutive model of shape memory alloy considering plasticity. Mechanics of Materials 48, 71 – 81. URL: http://www.sciencedirect.com/science/article/pii/

S0167663612000233, doi:https://doi.org/10.1016/j.mechmat.2012.02.001.

Ziólkowski, A., 2007. Three-dimensional phenomenological thermodynamic model of pseudoelasticity of shape memory alloys at finite strains. Continuum Mechanics and Thermodynamics 19, 379–398. URL: https://doi.org/10.1007/s00161-007-0060-y, doi:10.1007/s00161-007-0060-y.

Appendix

Nomenclature

A	constant regulating the drop of the upper and lower plateaus induced by fatigue and plastic accumulation during cycling loads
A_f	austenite finish temperature
B	constant regulating the drop of the lower plateau induced by plastic accumulation during cycling loads
b	scalar coefficient weighting the plastic strain effects on phase transformation domain size
$\mathbf{e}$	deviatoric strain tensor
$\mathbf{e}^{tr}$	phase transformation strain tensor
$\mathbf{e}^{fix}$	fatigue accumulated strain tensor
$\mathbf{e}^{pl}$	plastic strain tensor
F_1	transformation domain limit function
F_2	elastic domain limit function
G	shear modulus
h_1	first slope of the the transformation-induced hardening when $\parallel \mathbf{e}^{tr} \parallel < \varepsilon_L$
h_2	second slope of the the transformation-induced hardening when $\parallel \mathbf{e}^{tr} \parallel \geq \varepsilon_L$
h_2'	second slope of the transformation-induced hardening varying according to $\|\boldsymbol{\xi}\|$, $\varepsilon_L(t)$
h'	parameter linking h_1 and the entity of accumulated irreversible strain
$h_1^{'} = h_1 + h^{'}(\omega(t) + \eta(t))$	modified first slope of the the transformation-induced hardening due to inelastic strain accumulation
H_I	isotropic hardening coefficient for plastic strain
K	bulk modulus
k	scalar coefficient weighting the fatigue strain effects on phase transformation domain size
M_f	martensite finish temperature
$p = \frac{\partial \Psi}{\partial \theta}$	hydrostatic pressure
$\mathbf{Q} = -\frac{\partial \Psi}{\partial \mathbf{e}^{pl}}$	$\mathbf{e}^{pl}$ conjugate quantity
R	initial radius of the transformation domain
R_1'	modified radius of the transformation domain due to inelastic strain accumulation
R_2	initial radius of the yield surface
R_2'	modified radius of the yield surface due to isotrpic hardening
$\mathbf{s} = \frac{\partial \Psi}{\partial \mathbf{e}}$	deviatoric stress tensor
s_D^S	deviatoric stresses of forward transformation start
s_I^E	deviatoric stresses of inverse transformation end
T	actual temperature
T_0	reference temperature
$\mathbf{X} = -\frac{\partial \Psi}{\partial \mathbf{e}^{tr}}$	relative stress tensor
$\mathbf{Y} = -\frac{\partial \Psi}{\partial \mathbf{e}^{fix}}$	$\mathbf{e}^{fix}$ conjugate quantity

α	thermal expansion coefficient
β	constant in the chemical free energy term
$\boldsymbol{\varepsilon}$	total strain tensor
ε_{L0}	transformation plateau length at the the initial time t_0
ε_L	modified transformation plateau length due to inelastic strain accumulation
$\dot{\zeta}$	consistency parameter for the transformation domain limit function
$\eta(t) = \int_0^t \left\| \dot{\boldsymbol{e}^{pl}} \right\| dt$	accumulation of plastic strain in time
θ	volumetric strain
$\dot{\mu}$	consistency parameter for the elastic domain limit function
$\boldsymbol{\xi} = \mathbf{e}^{tr} - \mathbf{e}^{fix} - b\mathbf{e}^{pl}$	recoverable transformation strain during cycle
$\tau_M = \beta(T - M_f)$	chemical free energy term at the the initial time t_0
τ'_M	modified chemical free energy term due to inelastic strain accumulation
Φ	constant limiting the drop of the lower plateau with respect to the upper plateau
Ψ	Helmholtz free energy function
$\omega(t) = \int_0^t \left\| \dot{\boldsymbol{e}^{fix}} \right\| dt$	accumulation of fatigue strain in time